

Review

# Metal Chalcogenides Based Heterojunctions and Novel Nanostructures for Photocatalytic Hydrogen Evolution

Jian Li <sup>1</sup>, Pablo Jiménez-Calvo <sup>2</sup> , Erwan Paineau <sup>2,\*</sup>  and Mohamed Nawfal Ghazzal <sup>1,\*</sup>

<sup>1</sup> Institut de chimie physique, UMR 8000, CNRS, Université Paris-Saclay, 91405 Orsay, France; jian.li@u-psud.fr

<sup>2</sup> Laboratoire de Physique des Solides, CNRS, Université Paris-Saclay, 91405 Orsay, France; pablo.jimenez-calvo@u-psud.fr

\* Correspondence: erwan-nicolas.paineau@u-psud.fr (E.P.); mohamed-nawfal.ghazzal@u-psud.fr (M.N.G.)

Received: 16 December 2019; Accepted: 3 January 2020; Published: 7 January 2020



**Abstract:** The photo-conversion efficiency is a key issue in the development of new photocatalysts for solar light driven water splitting applications. In recent years, different engineering strategies have been proposed to improve the photogeneration and the lifetime of charge carriers in nanostructured photocatalysts. In particular, the rational design of heterojunctions composites to obtain peculiar physico-chemical properties has achieved more efficient charge carriers formation and separation in comparison to their individual component materials. In this review, the recent progress of sulfide-based heterojunctions and novel nanostructures such as core-shell structure, periodical structure, and hollow cylinders is summarized. Some new perspectives of opportunities and challenges in fabricating high-performance photocatalysts are also discussed.

**Keywords:** photocatalysis; water splitting; hydrogen; heterojunctions; porous structures; photonic crystals; imogolite nanotubes; noble-free materials; nanoparticles

## 1. Introduction

Solar energy is one of the most promising renewable energies because of its associated amount of energy density arriving to the earth surface, reported at 36000 TW (Department of Energy Report, “Solar Energy Utilization”). Considering that the population is reaching approximately nine billion for 2050 with an expected consumption of 28 TW, harvesting and storing solar energy is regarded as a suitable solution [1]. Photocatalysis is a state-of-the-art technology that can harvest solar energy and undergo chemical transformations to generate solar fuels, especially hydrogen (H<sub>2</sub>), which is a key vector for the foreseen low-carbon economy due to its high energetic density ca. 142 MJ/kg [2,3]. Photocatalyst is the most important factor in the photocatalysis process. Nevertheless, up to date, the photoconversion of most efficient catalysts for photocatalytic H<sub>2</sub> evolution is still far behind the level of large-scale applications.

The drawbacks of heterogeneous photocatalytic H<sub>2</sub> evolution are well identified as low light absorption, fast charge carrier recombination, short charge carrier lifetimes, and low conversion rates of the coordinate molecules [4–6]. For these reasons, the ideal photocatalysts should possess three main characteristics: (1) high light harvesting/absorption, (2) efficient charge carriers separation and transport, as well as (3) fast surface catalytic reactions. For this purpose, nanostructured semiconductors are of great interest for the photocatalytic hydrogen production. The possible orientation of the rational design of nanostructures to match structural, optical, morphological, and electronic properties should focus on modifying the energy band edges alignment with new energetic hybridization states to target more efficient redox reaction rates and effective sensitization of high-performance semiconductor

materials (SC) to simultaneously enhance light harvesting and charge carriers separation. In this direction, the formation of multi-phase heterojunctions or some peculiar nanostructures offer new opportunities in this growing field.

Multi-phase heterojunctions containing at least two materials are compelling engineering strategies in the materials chemistry field [7–11]. Staggered heterojunctions couple wide and narrow band gap semiconductors to drive rates of charge formation and separation at various interfaces along the photon to chemical product. These heterojunctions can be classified as the Z-scheme system and the Schottky junction system (Figure 1). Establishment of Z-scheme couplings between A/B introduces an effective strategy to tackle recombination of charges. The Z-scheme principle consists of the transfer of the electrons in the conduction band (CB) (A) to the valence band (VB) of B to combine with holes, while the electrons in the CB (B) reduce  $\text{H}_2\text{O}$  into  $\text{H}_2$ , and the holes in the VB (A) oxidize  $\text{H}_2\text{O}$  into  $\text{O}_2$  [12,13]. Schottky junction is another promising method to promote the separation of photogenerated electron–hole pairs [14,15]. The coupling of semiconductor and metallic nanoparticles lead to the formation of a space charge layer at the interface and an alignment of the fermi level energy, which results in Schottky junctions between the semiconductor and the co-catalysts. The Schottky junction enables efficient separation of the photogenerated electrons and promotes the photocatalytic activity. In this system, electrons can transfer from the photocatalyst to the co-catalyst via the aligned fermi level, which leads to the spatial charge separation, where the positive-charges are accumulated on the semiconductor and negative-charges on the co-catalyst.

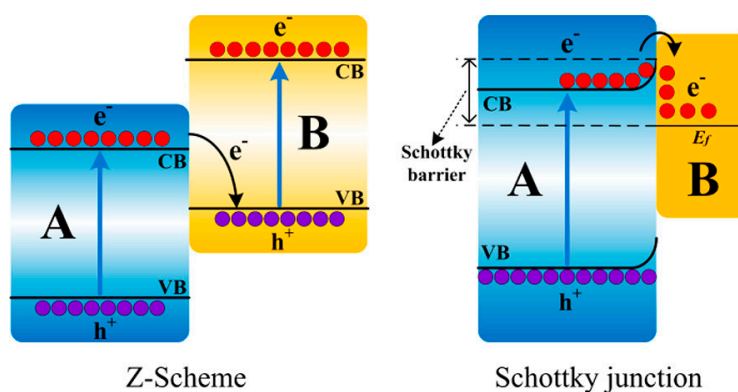


**Figure 1.** Schematic diagram of charge transfer for Z-scheme and Schottky junction systems. Adapted with permission from [7].

Compared to metal oxides, sulfides-based materials associated with polyvalent atoms (e.g., Cu, Ni, Fe, Co) are characterized as narrow band gap semiconductors, giving them a capacity of light absorption in the visible range [16,17]. Their band gap can be modified through a distinctive electron cascade mechanism present in these materials to reduce recombination and improve the separation of charge carriers. This objective can be achieved by using metal doping strategies such as cationic, anionic, or co-doping whilst maintaining a similar band gap. Therefore, the electronic and the optical properties are predictable by a rational selection of metals for promoting new hybrid materials [18].

Moreover, novel nanostructures such as core-shell structure, periodical structure, and hollow cylinders also display great potential for photocatalytic applications in analogy to heterojunctions [19,20]. The confinement of the light in 3D core-shell structures can reinforce the electromagnetic field at the nanostructure surface, which leads to the improved light harvesting for better photon to energy conversion. Periodically structured optical medium (due to multiple Bragg scattering) has also been identified as an efficient way to control light propagation and, in particular, the frequency-wavevector dispersion relation, i.e., the photonic band structure. A promising alternative is to develop hollow cylinders with permanent polarization, allowing a real-space band edges separation across their wall, which would provide a new one-dimensional semiconductor type to be used in photocatalysis.

Based on the above discussion, this review aims to focus on sulfides-based heterojunctions and novel nanostructures with distinctive physical-chemical properties. Firstly, we summarize the recent progress of CuS and NiS based heterojunctions for photocatalytic H<sub>2</sub> evolution classified by the “binary heterojunctions” and the “polynary heterojunctions”. Next, we introduce the TiO<sub>2</sub> based core-shell structure and periodical structure. Thirdly, we give as promising materials a brief introduction of imogolite nanotubes, a clay hollow cylinder, and their potential application for photocatalysis. Finally, some challenges and perspectives for the elaboration of high-performance photocatalysts are comprehensively analyzed, which might serve as reference for inspired future developments of photocatalysts.

## 2. Heterojunctions for Enhanced Charge Carriers Separation and Light Absorption

Hybrid photocatalysts consisting of at least two materials are considered as a promising system to increase the quantum efficiency of photocatalytic or photoelectrochemical reactions [21–24]. The strategy aims to reach either spatially separated charge carriers, extending the light absorption spectrum or accelerating the catalytic reaction kinetics. Compared to metal oxides, metal chalcogenides not only possess diverse architectures that can be enriched by integrating different metal ions and templates but also have narrow band gaps and suitable band positions that can be tuned through composition regulation (Figure 2) [16,17]. Owing to these attributes, metal chalcogenides-based heterojunctions as efficient photocatalysts have been actively explored. As a class of important p-type semiconductors, CuS possesses various stoichiometric compositions, valence states, and narrow bandgap. Owing to these attributes, CuS is widely used for the formation of heterojunctions to increase the absorption of composite materials in the visible region and thus improve the utilization of solar energy. In addition, due to the relatively high content of Ni element in the crust, NiS compounds are widely used as co-catalysts for photocatalytic application. In this section, the recent progress in fabricating CuS and NiS based heterojunctions for photocatalytic H<sub>2</sub> are summarized, which are classified as binary heterojunctions and polynary heterojunction.

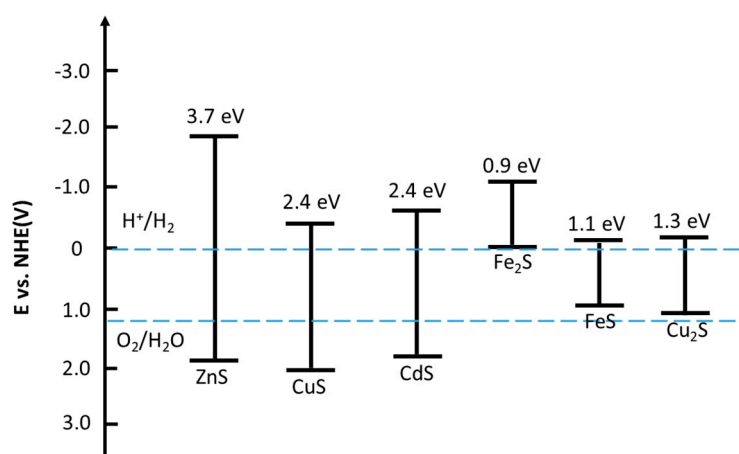


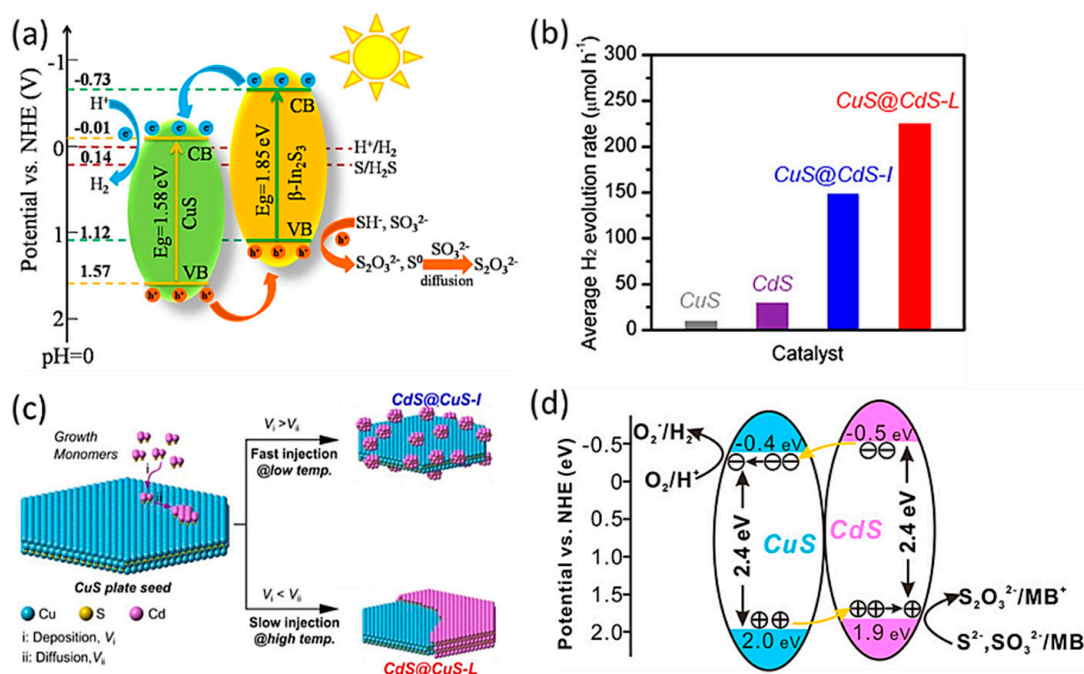
**Figure 2.** Schematic diagram illustrating the band gap, the potential energy of the conduction, and the valence band of promising metal chalcogenides.

### 2.1. Metal Chalcogenides Based Binary Heterojunctions

To date, many metal chalcogenides-based binary heterojunctions have been successfully prepared and used for the photocatalytic hydrogen evolution, where the heterojunction between the two materials plays an important role in the photocatalytic performance. In the following section, we review the recent progress of CuS- and NiS-based binary heterojunctions for photocatalytic hydrogen evolution.

### 2.1.1. CuS-Based Binary Heterojunctions

Arvind et al. fabricated hierarchical  $\text{In}_2\text{S}_3/\text{CuS}$  photocatalysts via a facile hydrothermal method (Figure 3a) [25]. The heterojunction showed superior visible light activity for  $\text{H}_2\text{S}$  splitting with a maximum  $\text{H}_2$  production rate of  $14950 \mu\text{mol g}^{-1} \text{h}^{-1}$  and an apparent quantum yield of 9.3% at 420 nm (Table 1). Such activity was attributed to the superior visible light absorption ability and matched energy level, which efficiently facilitated electron transfer between interfaces of  $\beta\text{-In}_2\text{S}_3$  and CuS. Liu et al. successfully prepared a series of shaped  $\text{CuS@CdS}$  core-shell hetero-junctions [26], which was achieved by using conformal CuS nanoplate seeds and a syringe pump to control the reaction kinetics. Two distinct growth patterns including island growth ( $\text{CuS@CdS-I}$ ) and layer-by-layer growth ( $\text{CuS@CdS-L}$ ) (Figure 3c) were demonstrated, and the  $\text{CuS@CdS-L}$  exhibited a better photocatalytic activity for hydrogen evolution (Figure 3b), which resulted from the intimate heterojunction structure (Figure 3d) and the high crystallinity of CdS. This work provides a versatile method for the rational design and synthesis of shape-dependent heterojunctions.

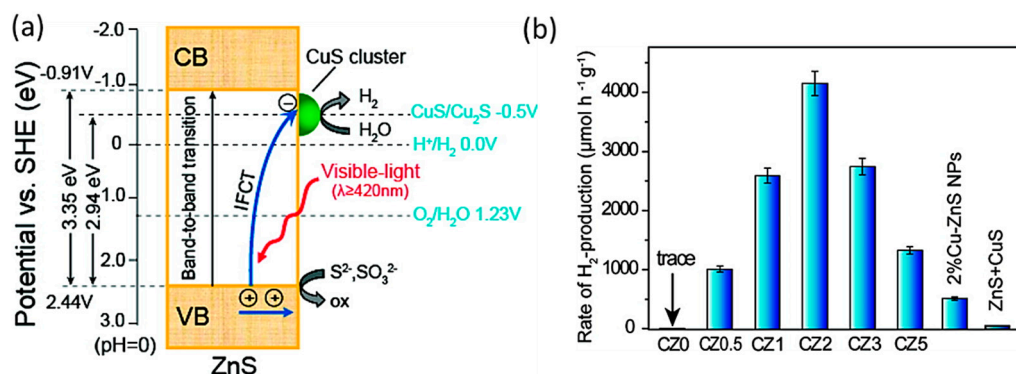


**Figure 3.** (a) Photocatalytic process of  $\text{In}_2\text{S}_3/\text{CuS}$  composites under visible light irradiation. Adapted with permission from [25]; (b) the  $\text{H}_2$  evolution rate by CuS, CdS,  $\text{CuS@CdS-I}$ , and  $\text{CuS@CdS-L}$  photocatalysts; (c) schematic illustration about the growth of CdS on CuS nanoplate seeds with two different routes; (d) the energy band structure of CuS and CdS. Adapted with permission from [26].

Zhang et al. constructed porous  $\text{CuS}/\text{ZnS}$  nanosheets via hydrothermal treatment and cation exchange reactions between  $\text{ZnS}(\text{en})_{0.5}$  nanosheets and  $\text{Cu}(\text{NO}_3)_2$  (Figure 4a) [27]. The prepared  $\text{CuS}/\text{ZnS}$  composites showed excellent photocatalytic hydrogen evolution activity under visible light, and the best  $\text{H}_2$ -production rate reached  $4147 \mu\text{mol h}^{-1} \text{g}^{-1}$  with quantum efficiency of 20% at 420 nm (Figure 4b). It was noted that photo-induced interfacial charge transfer (IFCT) occurred from the VB of ZnS to CuS, which led to partial reduction of CuS to  $\text{Cu}_2\text{S}$ . The interfacial transition energy from the VB of ZnS (+2.44 V) to  $\text{CuS}/\text{Cu}_2\text{S}$  (-0.5 V) was determined to be  $\sim 2.94 \text{ eV}$ , which thus absorbed the wavelength from  $\sim 350$  to 450 nm. This work shows a possibility to improve hydrogen-evolution activity by photo-induced IFCT.

**Table 1.** Summary of CuS and NiS based heterojunctions for photocatalytic H<sub>2</sub> evolution. CQDs refers to Carbon Quantum Dots.

Photocatalysts	Sacrificial Agent	HER Rate	Stability	Ref
In <sub>2</sub> S <sub>3</sub> /CuS	Na <sub>2</sub> S/Na <sub>2</sub> SO <sub>3</sub> along with 3M H <sub>2</sub> S	14,950 μmol g <sup>-1</sup> h <sup>-1</sup>	13 h	[25]
CuS@CdS	Na <sub>2</sub> S/Na <sub>2</sub> SO <sub>3</sub>	11,140 μmol g <sup>-1</sup> h <sup>-1</sup>	100 h	[26]
CuS/ZnS	Na <sub>2</sub> S/Na <sub>2</sub> SO <sub>3</sub>	4147 μmol g <sup>-1</sup> h <sup>-1</sup>	No data	[27]
NiS/TNTs	methanol	7486 μmol g <sup>-1</sup> h <sup>-1</sup>	No data	[28]
NiS/NBTNs	methanol	3170 μmol g <sup>-1</sup> h <sup>-1</sup>	14 h	[29]
NiS/CdS	lignin and lactic acid	1512.4 μmol g <sup>-1</sup> h <sup>-1</sup>	15 h	[30]
NiS/ZnIn <sub>2</sub> S <sub>4</sub>	Na <sub>2</sub> S/Na <sub>2</sub> SO <sub>3</sub>	2094 μmol g <sup>-1</sup> h <sup>-1</sup>	15 h	[31]
NiS/HNb <sub>3</sub> O <sub>8</sub>	Triethanolamine (TEOA)	1519.4 μmol g <sup>-1</sup> h <sup>-1</sup>	28 h	[32]
NiS/Zn <sub>x</sub> Cd <sub>1-x</sub> S	Na <sub>2</sub> S/Na <sub>2</sub> SO <sub>3</sub>	16780 μmol g <sup>-1</sup> h <sup>-1</sup>	20 h	[33]
NiS/C <sub>3</sub> N <sub>4</sub>	TEOA	482 μmol g <sup>-1</sup> h <sup>-1</sup>	24 h	[34]
ZnMoS <sub>4</sub> /ZnO/CuS	Na <sub>2</sub> S/Na <sub>2</sub> SO <sub>3</sub>	38,220 μmol g <sup>-1</sup> h <sup>-1</sup>	8 h	[35]
CuS/CdIn <sub>2</sub> S <sub>4</sub> /ZnIn <sub>2</sub> S <sub>4</sub>	Na <sub>2</sub> S/Na <sub>2</sub> SO <sub>3</sub>	358.4 μmol g <sup>-1</sup> h <sup>-1</sup>	No data	[36]
NiS/CdS/TiO <sub>2</sub>	Na <sub>2</sub> S/Na <sub>2</sub> SO <sub>3</sub>	2149 μmol g <sup>-1</sup> h <sup>-1</sup>	16 h	[37]
CQDs/NiS/ZnIn <sub>2</sub> S <sub>4</sub>	TEOA	600 μmol g <sup>-1</sup> h <sup>-1</sup>	15 h	[38]
NiS/CDs/CdS	Na <sub>2</sub> S/Na <sub>2</sub> SO <sub>3</sub>	1444.5 μmol g <sup>-1</sup> h <sup>-1</sup>	15 h	[39]

**Figure 4.** (a) Schematic illustration of interfacial charge transfer (IFCT) from the valence band of ZnS to the CuS clusters in CuS/ZnS system; (b) comparison of the H<sub>2</sub>-production activity of CuS/ZnS with different molar ratio and ZnS samples under visible light in a mixed solution with 0.35 M Na<sub>2</sub>S and 0.25 M Na<sub>2</sub>SO<sub>3</sub> as sacrificial agent. Adapted with permission from [27].

### 2.1.2. NiS-Based Binary Heterojunctions

Huang et al. prepared NiS loaded TiO<sub>2</sub> nanotubes (TNTs) by a simple solvothermal method (Figure 5a) [28]. NiS as co-catalyst can significantly improve the photocatalytic activity for H<sub>2</sub> evolution, and the content of NiS played a crucial role in the performance. The optimal heterojunction led to a hydrogen production rate of ~7486 μmol/h/g, which was 79 times higher than that of pure TNTs, which indicates NiS is a promising co-catalyst to boost photocatalytic activity (Figure 5b). Qiao et al. prepared NiS nanoparticles modified black TiO<sub>2</sub> hollow nanostructure (NBTNs) via surface hydrogenation and hydrothermal reaction (Figure 5c) [29]. The resultant NBTNs exhibited a preminent photocatalytic H<sub>2</sub> generation rate (3.17 mmol/h/g), which was comparable to the activity of Pt loaded black TiO<sub>2</sub> (3.95 mmol/h/g). The superior activity was attributed to the synergistic effects of NiS co-catalyst and building Ti<sup>3+</sup> self-doping and oxygen vacancy. This unique structure provides more active sites and enhances the separation of photogenerated charge carrier with prolonged charge lifetime.

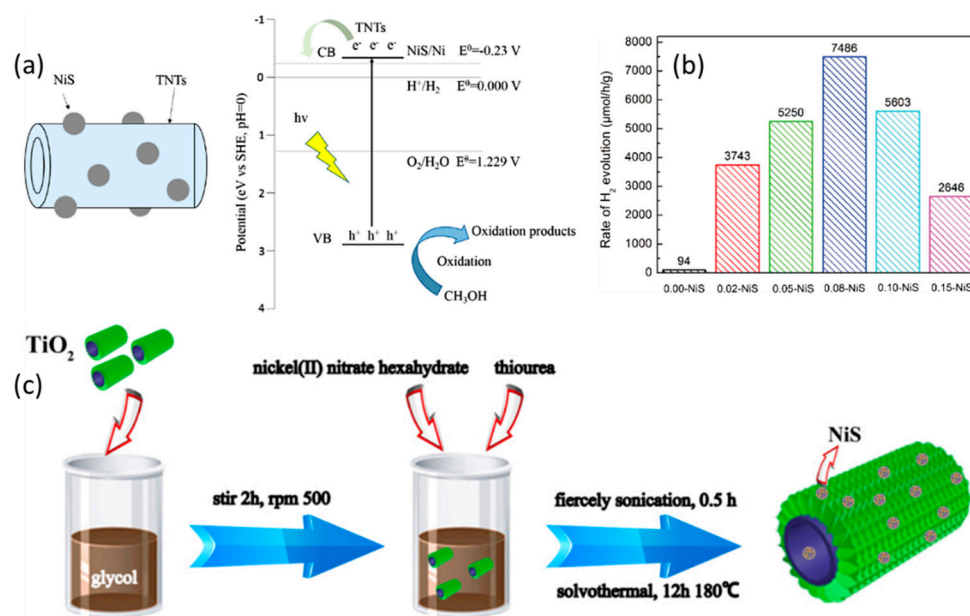


**Figure 5.** (a) Proposed charge transfer in NiS/ TiO<sub>2</sub> nanotubes (TNTs) photocatalyst under UV irradiation; (b) average hydrogen production of TNTs with different amounts of NiS. Adapted with permission from [28]; (c) schematic illustration of synthesis of the NiS nanoparticles modified black TiO<sub>2</sub> hollow nanostructure (NBTNs). Adapted with permission from [29].

Li et al. synthesized 1D NiS/CdS nanocomposites with different NiS loading weights by using a two-step solvothermal method (Figure 6a) [30]. The intimate contact between CdS and NiS enhanced charge carrier separation and promoted surface kinetics for H<sub>2</sub> production. As a result, the optimized NiS/CdS heterojunction exhibited superior hydrogen production rate of 1512.4 μmol h<sup>-1</sup> g<sup>-1</sup>, nearly 5041 times higher than that of bare CdS. Transient absorption (TA) techniques revealed that the 0.2 molar ratio of NiS loaded CdS nanowires (NWs) possessed the longest charge carrier lifetime. The increase in NiS loading resulted in a shorter lifetime due to the aggregation of NiS nanoparticles, which was consistent with the photocatalytic performance for hydrogen evolution (Figure 6b). NiS/ZnIn<sub>2</sub>S<sub>4</sub> nanocomposites were prepared via a two-step hydrothermal method by Li's group (Figure 6c) [31]. These nanocomposites showed an improved photocatalytic hydrogen evolution under visible light irradiation. The optimal hydrogen evolution rate reached 104.7 μmol h<sup>-1</sup>, which was even better than that of Pt loaded ZnIn<sub>2</sub>S<sub>4</sub> nanocomposite (77.8 μmol h<sup>-1</sup>). Xia et al. dispersed ultra-small NiS on HNb<sub>3</sub>O<sub>8</sub> nanosheets via a facile electrostatic adsorption/self-assembly process (Figure 6d) [32]. Compared to the traditional modification of NiS by co-precipitation and mechanical mixing methods, this approach could produce sub-nanometer sizes of NiS by the interlayered spatial steric inhibition effect. It induced strong interactions between NiS and HNb<sub>3</sub>O<sub>8</sub> nanosheets. As a result, the as-prepared composite achieved high H<sub>2</sub> evolution rate of 1519.4 μmol g<sup>-1</sup> h<sup>-1</sup>, which was one magnitude higher than that of the sample prepared by a mechanical mixing method and even comparable to the Pt/HNb<sub>3</sub>O<sub>8</sub>.

Zhao et al. developed a metal-organic framework (MOF)-template strategy to prepare co-catalyst/solid solution heterojunction NiS/Zn<sub>x</sub>Cd<sub>1-x</sub>S (Figure 7a) [33]. By adjusting the doping metal concentration in MOFs, the chemical compositions and the bandgaps of the heterojunctions could be fine-tuned, and the light absorption capacity and the photocatalytic activity were further optimized. The optimal NiS/Zn<sub>0.5</sub>Cd<sub>0.5</sub>S exhibited a hydrogen evolution rate of 16.78 mmol g<sup>-1</sup> h<sup>-1</sup> and high stability under visible light (λ > 420 nm) (Figure 7b). Density functional theory (DFT) calculations revealed the relationship between the heterojunction and the photocatalytic activity and confirmed the importance of NiS in accelerating the water dissociation kinetics, which is a crucial factor for photocatalytic hydrogen evolution reaction (HER). Hong et al. developed an NiS modified C<sub>3</sub>N<sub>4</sub>

photocatalyst by using a simple hydrothermal method (Figure 7c) [34]. Both the loading weight of NiS and the reaction temperature had large effects on the photocatalytic hydrogen evolution rate. The optimal NiS/C<sub>3</sub>N<sub>4</sub> photocatalyst reached 48.2 mmol/h, which was 253 times higher than that of bare C<sub>3</sub>N<sub>4</sub> and could maintain nearly 80% activity after four runs of 24 h. This study demonstrates that NiS could also improve photocatalytic activity of polymeric semiconductor.

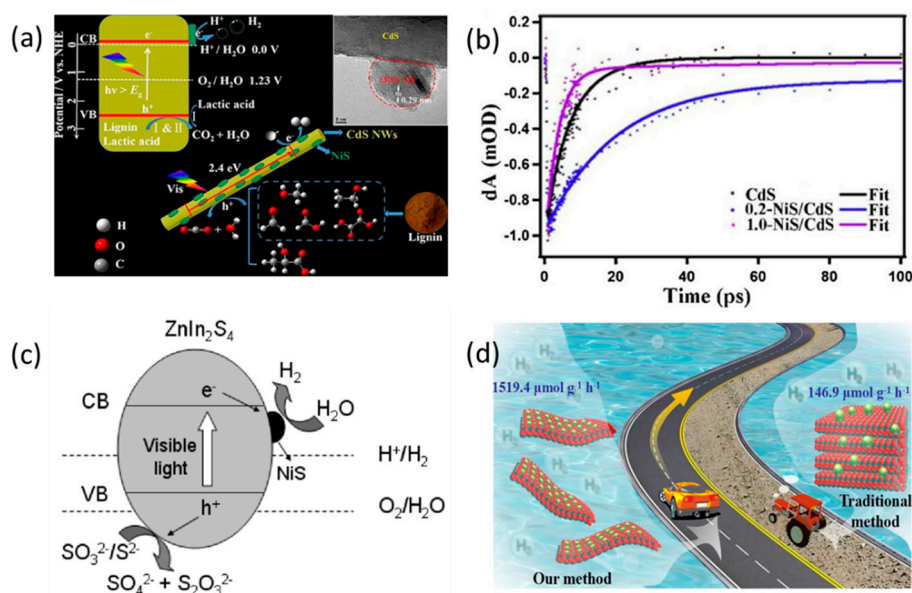


**Figure 6.** (a) Schematic illustration of the photocatalytic hydrogen production by NiS/CdS composites; (b) normalized ultrafast transient bleach decay of CdS nanowire, 0.2-NiS/CdS and 1.0-NiS/CdS. Adapted with permission from [30]; (c) schematic illustration of proposed mechanism over NiS/ZnIn<sub>2</sub>S<sub>4</sub> photocatalysts. Adapted with permission from [31]; (d) comparison of NiS/HNb<sub>3</sub>O<sub>8</sub> photocatalysts synthesized by electrostatic adsorption method and traditional method. Adapted with permission from [32].

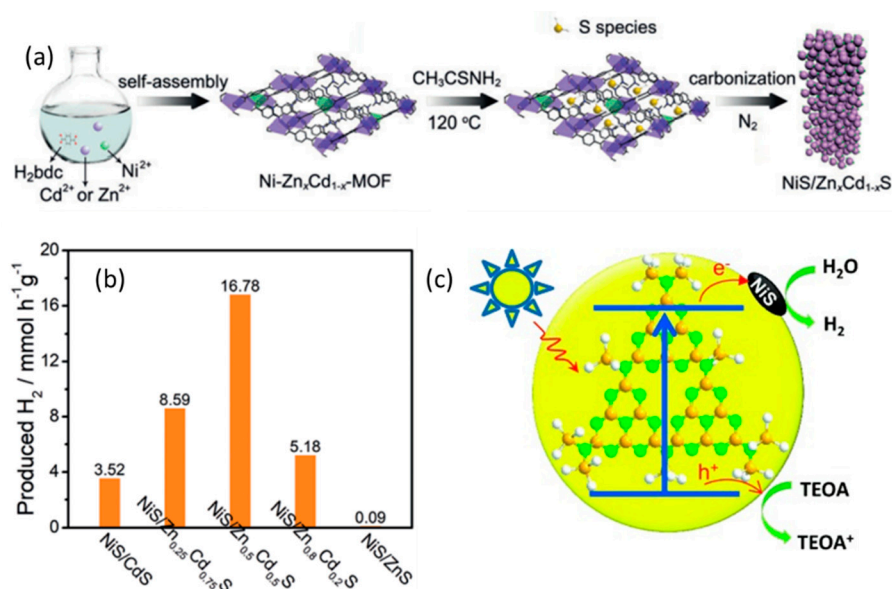


**Figure 7.** (a) Schematic illustration of the synthetic procedure for NiS/Zn<sub>x</sub>Cd<sub>1-x</sub>S; (b) comparison of H<sub>2</sub>-evolution rates of NiS/Zn<sub>x</sub>Cd<sub>1-x</sub>S under visible-light irradiation. Adapted with permission from [33]; (c) schematic illustration of photocatalytic hydrogen evolution of NiS/C<sub>3</sub>N<sub>4</sub>. Adapted with permission from [34].

## 2.2. Metal Chalcogenides Based Polynary Heterojunctions

Compared to binary heterojunctions, the polynary heterojunctions lead to a higher photocatalytic activity because of the multiple separations of photogenerated carriers driven by the energy band alignments. Thus, plenty of metal chalcogenides based polynary heterojunctions have been studied for photocatalytic hydrogen evolution. In the following part, we focus on the progress of CuS and NiS based polynary heterojunctions for photocatalytic hydrogen evolution.

### 2.2.1. CuS Based Polynary Heterojunctions

Ho et al. developed multiple ZnMoS<sub>4</sub>/ZnO/CuS heterojunctions (Figure 8b) [35]. In the structure, the middle ZnO layer could induce interfacial band bending, which facilitated electron transfer from ZnMoS<sub>4</sub> across the multi-junction heterostructures to the surface of CuS for hydrogen evolution. The optimized configuration achieved a hydrogen evolution rate of 38.22 mmol g<sup>-1</sup> h<sup>-1</sup>, which was twice as much as the ZnMoS<sub>4</sub>/CuS heterojunction (Figure 8a). This work offers a band structure engineering strategy to fabricate highly efficient photocatalysts. Chen et al. constructed CuS/CdIn<sub>2</sub>S<sub>4</sub>/ZnIn<sub>2</sub>S<sub>4</sub> photocatalysts via a microwave assisted one-step method (Figure 8c) [36]. The hybrid composite possessed a large surface area and visible light response with an absorption edge of ~670 nm. After loading Pt as the co-catalyst, the CuS/CdIn<sub>2</sub>S<sub>4</sub>/ZnIn<sub>2</sub>S<sub>4</sub> photocatalysts achieved a hydrogen production rate of 358.4 μmol h<sup>-1</sup> g<sup>-1</sup> under simulated sunlight and a hydrogen production rate of 233.9 μmol h<sup>-1</sup> g<sup>-1</sup> under visible light (λ > 420 nm), which were much better than those of bare P25 and ZnIn<sub>2</sub>S<sub>4</sub>. Such a performance was ascribed to the enlargement of visible light response and the increase of the pathways for photo-generated carrier migration.

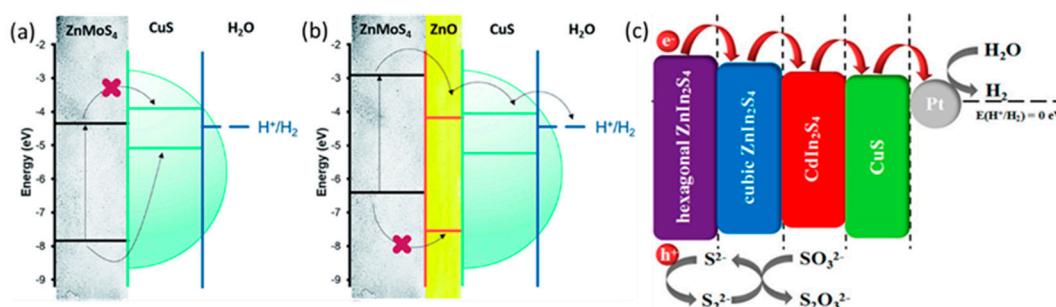


**Figure 8.** Electronic band alignments relative to water redox potentials and possible transfer routes of electrons and holes in (a) ZnMoS<sub>4</sub>/CuS and (b) ZnMoS<sub>4</sub>/ZnO/CuS. Adapted with permission from [35]; (c) energy band structure and corresponding photocatalytic reaction mechanism for H<sub>2</sub> production over the CuS/CdIn<sub>2</sub>S<sub>4</sub>/ZnIn<sub>2</sub>S<sub>4</sub> composite in Na<sub>2</sub>S–Na<sub>2</sub>SO<sub>3</sub> aqueous solution. Adapted with permission from [36].

### 2.2.2. NiS-Based Polynary Heterojunctions

Li et al. synthesized hollow NiS/CdS/TiO<sub>2</sub> (NS/CT) photocatalysts by using a metal-organic framework as a template (Figure 9a) [37]. Such heterojunction could not only enhance the visible light absorption but also provided smooth transfer pathways for the electrons, thus facilitating the photo-generated carrier separation. As a result, the optimal photocatalysts achieved a hydrogen evolution rate of 2149.15 μmol g<sup>-1</sup> h<sup>-1</sup>, which was much better than that of pure CdS and CdS/TiO<sub>2</sub>, respectively (Figure 9b). This work provides a novel and facile synthesis approach to fabricate high-efficiency photocatalysts. Wang et al. constructed a ternary nanocomposite via self-assembly of ZnIn<sub>2</sub>S<sub>4</sub> microspheres on the surface of NiS/carbon quantum dots (CQDs) (Figure 9c) [38]. The as-prepared photocatalysts showed superior photocatalytic activity with a hydrogen evolution rate of 2149.15 μmol g<sup>-1</sup> h<sup>-1</sup>, much better than that of ternary CQDs/NiS/ZnIn<sub>2</sub>S<sub>4</sub>, which was synthesized by deposition of NiS on the surface of CQDs/ZnIn<sub>2</sub>S<sub>4</sub> (Figure 9d). Such enhancement of ternary CQDs/NiS/ZnIn<sub>2</sub>S<sub>4</sub> is ascribed to the introduction of CQDs, which acted as a bridge to promote

the electron transfer from  $\text{ZnIn}_2\text{S}_4$  to NiS. This study indicated rational design and elaboration of ternary CQDs-based systems show great potential in fabricating highly efficient photocatalytic hydrogen evolution.

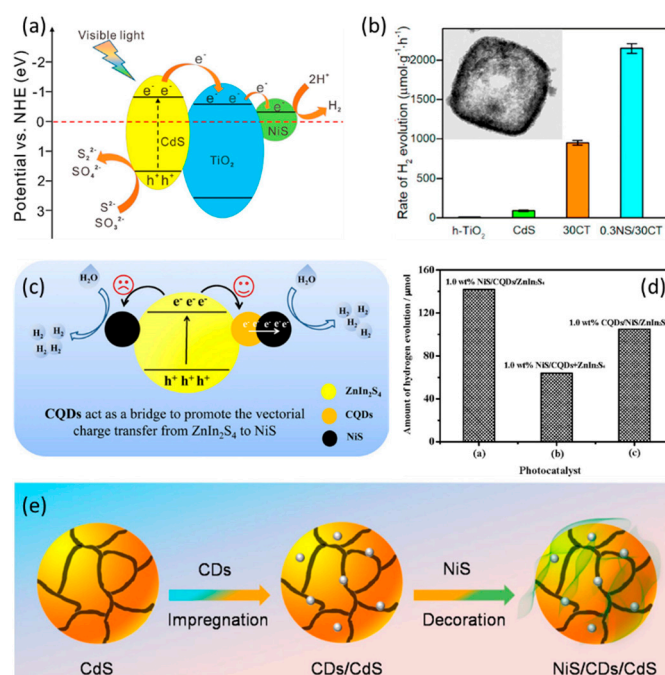


**Figure 9.** (a) Schematic illustration of the photocatalytic mechanism on NiS/CdS/TiO<sub>2</sub> photocatalysts; (b) the corresponding H<sub>2</sub> evolution rate of the samples. Adapted with permission from [37]; (c) proposed mechanism over NiS/CQDs/ZnIn<sub>2</sub>S<sub>4</sub> nanocomposite for hydrogen evolution; (d) the amount of evolved H<sub>2</sub> over different samples. Adapted with permission from [38]; (e) schematic illustration for the synthesis of NiS/CDs/CdS photocatalyst. Adapted with permission from [39].

Similarly, ternary NiS/CDs/CdS photocatalysts were rationally designed and successfully synthesized by Liu's group (Figure 9e) [39]. After adjusting the loading ratio of NiS and CDs, the optimal composite exhibited a hydrogen evolution rate of 1444.5 μmol h<sup>-1</sup> g<sup>-1</sup> under visible light, which was much higher than that of bare NiS/CdS and CDs/CdS. In the hybrids, the internal p–n junction between NiS and CdS facilitated the charge separation, and the middle CDs acted as electron reservoirs to extract electrons fast, thus further limiting the electron–hole recombination. This work paves a new pathway for the rational design of efficient hybrid photocatalysts toward solar energy conversion to chemical fuels.

### 3. 3D Nanostructure an Accelerator of the Photochemistry

Titanium dioxide in its anatase crystallographic phase is by far the most popular photocatalyst. However, TiO<sub>2</sub> has a large band gap (3.2 eV for anatase) that can be excited only by UV light, which lowers the solar energy conversion efficiency and prevents its use in the visible range (negligible absorbance factor). Furthermore, TiO<sub>2</sub> strongly suffers from high recombination rate of the photogenerated electron–hole pairs, which lowers its photoefficiency. Two strategies have been used to overcome the limitations due to these factors with some success. One consists of doping TiO<sub>2</sub> with non-metallic elements, such as C [40], N [41,42], S [43], B [42], etc., in order to lower the electronic band gap, and the other deals with coupling TiO<sub>2</sub> with a second photoactive compound, such as dye-based compounds [44,45] and semiconductors with a narrower band gap energy and a suitable potential energy [46–48]. Even if these strategies enable one to extend the absorbance of TiO<sub>2</sub> in the visible range, the stability of photoactive compounds and/or the efficiency of light harvesting remains limited.

Enhancing the light harvesting of the TiO<sub>2</sub> photocatalyst (absorbance factor) becomes a challenge, especially regarding the management of light propagation. The speed of light in the medium ranges around  $1\text{--}3 \times 10^8 \text{ m s}^{-1}$ , which implies about a hundred femtoseconds to pass through 10  $\mu\text{m}$  thick samples (and even less for TiO<sub>2</sub> nanoparticles in colloidal solution). The confinement of the light in the 3D structure has been reported as an efficient strategy to improve the light harvesting for better photon to energy conversion.

Spherical nanoparticles used as dielectric Mie resonators were reported as a new and promising system boosting the hydrogen production in plasmonic core-shell nanostructures. Gessesse et al. designed a plasmonic sub-micrometric core-shell nanostructure capable of light manipulation for higher photocatalytic production of hydrogen using a very low amount of Au nanoparticles (Figure 10a) [20]. The SiO<sub>2</sub>@Au@TiO<sub>2</sub> nanostructure mimics the role played by epidermal cells and act lens-like. The researchers showed that the Mie scattering dominates when the particle size is larger than a wavelength (Figure 10b). The Mie scattering produces complex field distribution patterns reminiscent of directional antennas. This effect is sometimes referred to as a photonic nanojet. From the point of view of geometrical optics, the increase in the scattering field intensity with a more intense forward lobe reflects the fact that a dielectric sphere with large size behaves as a convex lens. Thus, the core-shell nanostructure acts as a convex nano-lens reinforcing the electromagnetic field at the nanostructure surface (Figure 10d). The electric field was also found to be enhanced, which improved the energy absorbed for gold particles located near the shell surface. Tuning the size of the core-shell nanostructure improved the absorption and thus improved the photocatalytic hydrogen production (Figure 10c).

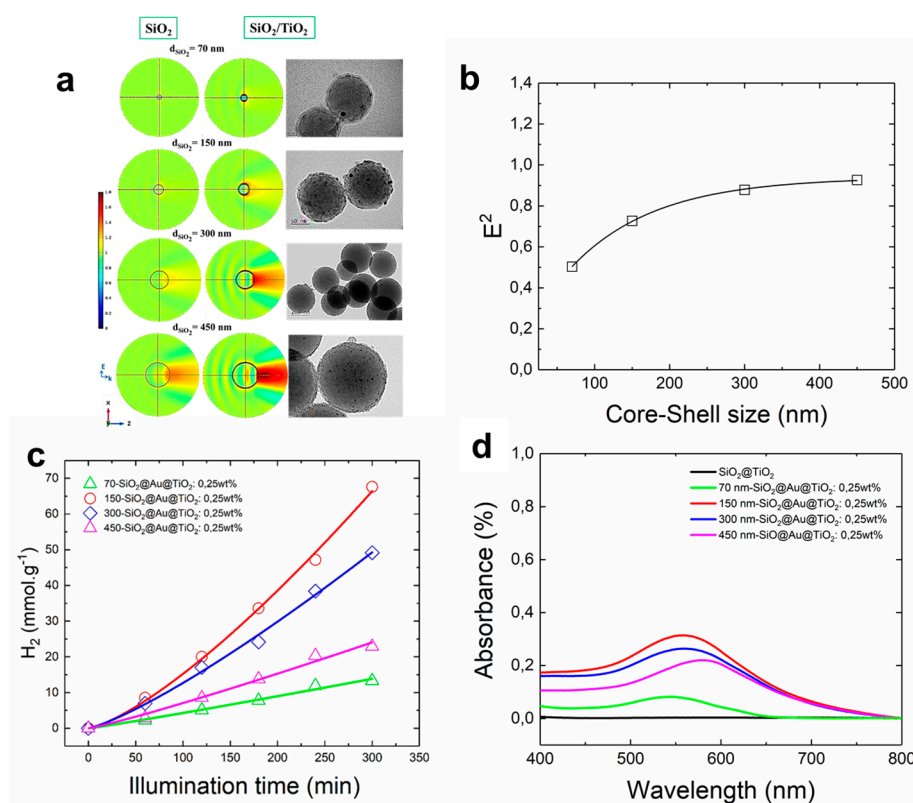


**Figure 10.** (a) Complex electric field distribution patterns for different diameters of silica core before (SiO<sub>2</sub>) and after (SiO<sub>2</sub>@TiO<sub>2</sub>) shell coating and their correspondent TEM images; (b) the squared electric field amplitude evolution vs. the core-shell size averaged over the plasmonic core-shell nanostructure; (c) the photocatalytic hydrogen generation under UV visible light irradiation for variable size of the core-shell plasmonic nanostructure (70 to 450 nm); (d) UV visible absorption spectra of plasmonic core-shell with variable silica core size.

Periodically structured optical medium (due to multiple Bragg scattering) has also been reported as an efficient strategy to control the light propagation and, in particular, the frequency-wavevector dispersion relation, i.e., the photonic band structure [49]. The pioneering work of Yablonovich [50] proposed the basics of the extraordinary properties of photonic crystals (PCs) (Figure 11a). Photonic crystals in nature, e.g., butterfly wing, weevil, or beetle cuticles, present amazing and complex structures that manage the propagation of light in such a perfect way that they produce iridescent colors [51,52]. PCs can be produced artificially either by alternating high and low refractive index materials [53,54] or by self-assembling spherical nanoparticles [55]. PCs designed from 1D, 2D, and 3D periodical arrangement of materials interact with electromagnetic radiation and inhibit the propagation of light in well-defined wavelength (energy) ranges and directions (photonic band gap) (Figure 11b). Many developments in waveguides [56], dielectric mirrors, sensors [57], and low threshold lasers [58] derive directly from the photonic band gap property. However, the propagation of light at the bandgap edges recently attracted attention in photocatalytic applications. At the lower photon energy edge (red edge) of the photonic bandgap, the light standing wave intensity peaks are primarily localized in the high refractive index dielectric regions of the PC, whereas at the higher photon energy edge (blue edge), they are primarily localized in the low refractive index dielectric regions. The group velocity of light ( $\vec{V}_g = \frac{\partial \omega}{\partial \vec{k}}$ ) is defined as the “local derivative” or the “slope” of the photonic band curve in the frequency  $\omega$  versus wave-vector  $\vec{k}$  diagram. Near the photonic band edges, this derivative tends to zero, i.e., the photonic band curve flattens. In other word, near the red-edge (or blue-edge) wavelength of the photonic band gap, the light is slowed down, justifying the term “slow photons”. The residence time of photons in the PCs increases considerably, which could improve the absorbance factor of the material. Kang’s group used the concept of “slow photon” to increase the photoefficiency of the Au/TiO<sub>2</sub> PCs structure [59]. The authors attributed such an enhancement to the improvement of the light harvesting due to the low group velocity of light near the red-edge of the “stop-band” (another name for photonic band gap). They reported that the enhancement of the photocatalytic efficiency was closely related to the position of the Bragg reflection peak wavelength with respect to the electronic band edge of TiO<sub>2</sub> (Figure 11e).

Recently, Gesesse et al. proposed the use of cellulose nanocrystals as a biotemplate to structure TiO<sub>2</sub> films in order to improve its light harvesting properties [19]. The authors use the capability of cellulose nanocrystals to organize themselves in chiral nematic structures to obtain a photonic film used as a biotemplate (Figure 12a,b). The proposed method enables one to synthesize TiO<sub>2</sub> films containing a replica of the chiral nematic structure. Under illumination, the charge carriers density was improved for the mesostructured films (Figure 12c). Particularly, the absorption factor of TiO<sub>2</sub> increase due to the multiple light scattering within the structured film resulted in higher photoefficiency. Introducing plasmonic nanoparticles (such as gold) in such a structure improves the plasmon intensity, which leads to higher photocatalytic production of H<sub>2</sub> (Figure 12d).

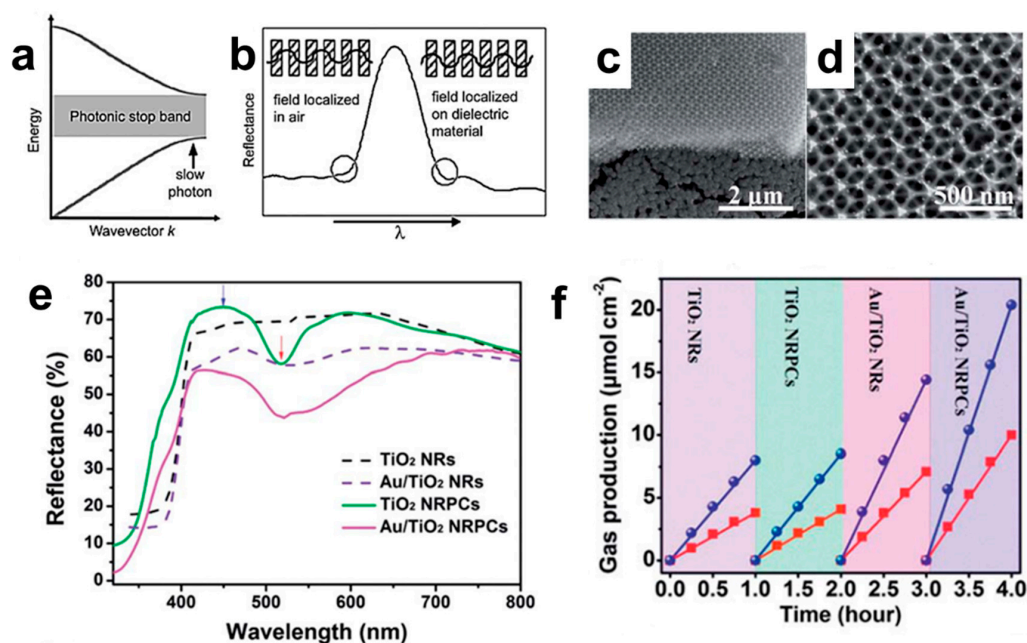


**Figure 11.** (a) Simplified scheme of optical photonic band gap of a photonic crystal; (b) the velocity of light slows down at the lower photon energy edge (red edge) and at the higher photon energy edge (blue edge) of the Bragg peak reflection (forbidden wavelength). Adapted with permission from [49]; (c) low-magnification and (d) high-resolution SEM images of ordered Au/TiO<sub>2</sub> inverse opal film; (e) reflectance spectra showing the Bragg peak reflection maxima obtained for different samples compared to the absorbance spectra of TiO<sub>2</sub>; (f) photocatalytic rate of hydrogen and oxygen generation over variable photocatalysts. Adapted with permission from [59].

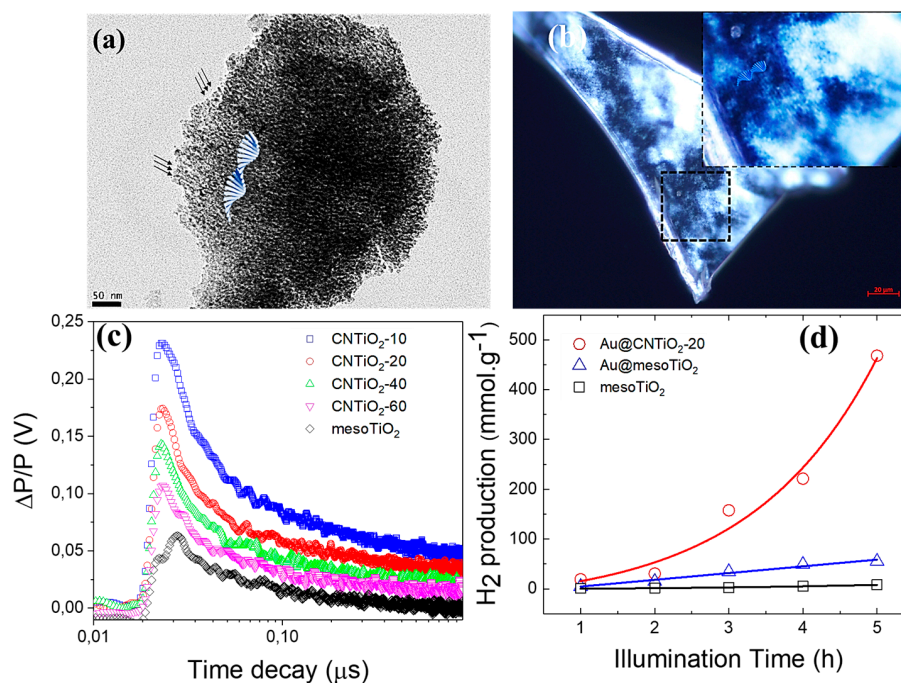


**Figure 12.** (a) TEM micrographs and (b) polarized optical microscopy images of TiO<sub>2</sub> film containing a replica of chiral nematic structure obtained by impregnation method; (c) Time-Resolved Microwave Conductivity (TRMC) signal of variable TiO<sub>2</sub> films under UV illumination showing the evolution of the charge carrier density produced upon UV laser excitation; (d) hydrogen production versus the illumination time showing the beneficial effect of chiral nematic structure on H<sub>2</sub> generation.

#### 4. Imogolite Clay Nanotubes (INT)

Tubular structures with tunable monodisperse diameters in the nanometer scale are attracting a lot of attention in nanosciences lately. In recent years, nanotubes have been recognized as an ideal 1D nano-platform appealing for applications to be potential catalytic nanoreactors for energy conversion application [60–62]. In parallel, synthesis of 2D and 3D nanostructures with permanent polarization has shown interesting activities due to their capacities of generation and separation of charge carriers ( $e^-/h^+$ ) [63], resulting in a new type of photoactive material [64]. To the best of our knowledge, the use of polarized, diameter-controlled nanotubes for carrying out the typical photocatalytic steps is a paradigm to explore but might set a landmark of a new generation of catalysts. This challenging and promising area requires understanding and control of the molecular interactions with the interface at the nanometer-scale, the photonic profile from the light activation source, and the heterogeneous catalysis of the nanoreactor.

##### 4.1. A Promising Tunable Nanoreactor

INTs appear in this context as promising functional nanostructures [65,66]. Belonging to clay minerals, imogolite is a naturally occurring aluminosilicate nanotube originally described in volcanic soils of Japan [67]. The structure of these nanotubes consists of a curved dioctahedral gibbsite-like layer where isolated tetrahedron units are connected upright to the octahedral vacancy by sharing three oxygen atoms (Figure 13).

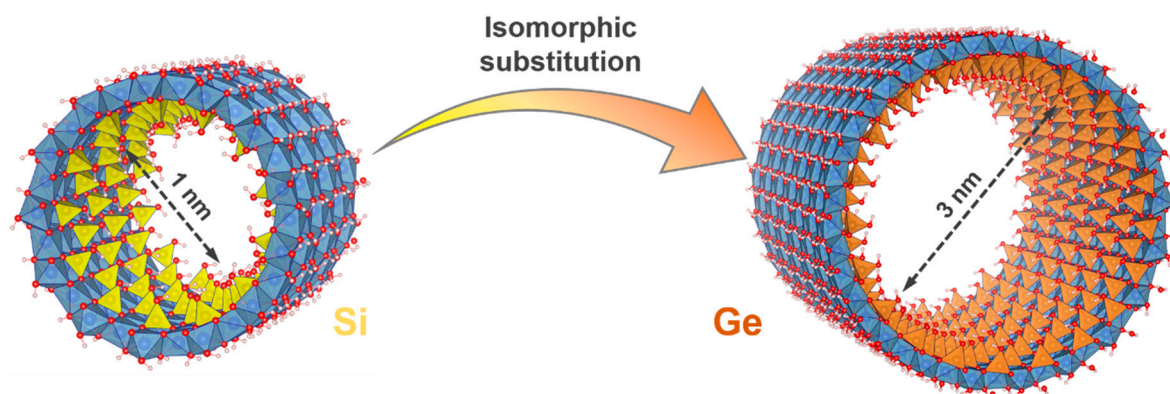
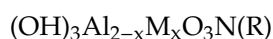


**Figure 13.** Structure and inner diameter size for the endmembers of single-walled imogolite clay nanotubes (INT) with nominal composition  $(OH)_3Al_2O_3Si_xGe_{1-x}(OH)$ . Color code: silicon (yellow); germanium (orange); aluminum (blue); oxygen (red); hydrogen (white).

However, INTs are widely dispersed in the environment, thus limiting their applications. The major breakthrough for using INTs was certainly their synthesis by sol-gel methods under mild conditions [68]. Moreover, INTs benefit from a well-defined minimum of strain energy [69,70], which allows the direct synthesis of nanotubes monodisperse in diameter [71,72] and chirality [73] with adjustable pore size (1–3 nm), shape (single-walled, SW, or double-walled, DW), and surface properties (hydrophilic or hydrophobic internal cavity) simply by isomorphous substitution (Figure 13) [74–79]. Isomorphous replacement of the outer octahedron atom ( $Al^{3+}$ ) and the internal tetrahedron sites ( $Si^{4+}$ ) with different transition metals or functional groups leads to a theoretical general formula of INT defined as [80]:



where  $M = Fe, F$ ;  $N = Si, Ge, As$ ;  $R = OH, CH_3, CH_2NH_2$ . The aim of replacing one of these two atoms (M or N sites) or even both simultaneously is to drive changes on the overall structure of the INTs (either in the external or in the internal surface), namely on structural, morphological, optical, and electronic properties that can be beneficial for their activity. Another important strategy of INT modification consists of functionalizing the outer surface with a different functional group. The high

density of hydroxyl groups on the outer surface of imogolite nanotubes ( $\sim 18 \text{ OH/nm}^2$ ) allows grafting polymers with specific functionalities to interact either by covalent or hydrogen bonding.

#### 4.2. Applications in (Photo)Catalysis

Owing to their peculiar structure, the inner and the outer surfaces of INTs present unique acid/base properties, offering different pathways for adsorption, catalytic reactions, and—to a lesser extent—photocatalysis. The purpose of this section is to provide the state-of-the-art of studies dealing with (photo)catalysis applications using INTs.

##### 4.2.1. Catalysis and Fenton Reaction

In a seminal paper, Farmer et al. suggested that the catalytic properties of INTs could be unique [81]. It was found shortly after that INTs may be suitable for hydrodemetalizing heavy oils and selectively hydroprocessing asphaltenes in crude oils [82]. Since then, several studies have demonstrated that INTs offer a wide range of uses in the isomerization of various molecules, such as 1-butene [83],  $\alpha$ -pinene [84], or glucose [85], to cite a few. Although the observed conversion rate is not significantly different from that obtained with conventional catalysts, these works can be regarded as proofs-of-concept on the use of INTs as catalysts with potential improvement through their structural modifications by either isomorphic substitution or functionalization. A promising step is the structural incorporation of transition metals in the outer wall of the nanotubes, typically by partial substitution of  $\text{Al}^{3+}$  with iron  $\text{Fe}^{3+}$  (or  $\text{Fe}^{2+}$ ) with low substitution ratio  $x = [\text{Fe}]/([\text{Fe}] + [\text{Al}])$  ( $x \leq 0.1$ ) to avoid the formation of by-products [86].

Ookawa and co-workers used Fe-doped INTs for catalytic oxidation with  $\text{H}_2\text{O}_2$  of different aromatic hydrocarbons compounds, such as phenol, cyclohexene, benzene, chlorobenzene, or benzaldehyde, to their respective isomers but with low selectivity [87,88]. In a similar approach, Shafia et al. followed the degradation of the azo-dye Acid Orange 7 (AO7) in the presence of  $\text{H}_2\text{O}_2$  and Fe-doped INTs [89]. The system achieved 90% dye removal from the solution after only 5 min of contact, suggesting that  $\text{Fe}^{3+}$  ions can coordinate the nitrogen atoms of AO7. Beyond isomorphic substitution, metal-loaded INT is another strategy for catalytic applications. Imamura et al. prepared a Cu-loaded INT as a binary catalyst for the decomposition of two peroxides with different molecular sizes, namely *tert*-butyl hydroperoxide and 1,1-bis (*tert*-butyldioxy)cyclodecane, which exhibit around 80% conversion after 100 and 300 min, respectively [90]. Supramolecular functionalization of imogolite with 3-aminopropyltriethoxysilane (3-APS) was employed to immobilize soluble catalysts such as osmium tetroxide (Figure 14a) [91]. The resulting ternary complex was tested for dihydroxylation of a wide range of olefin species, but despite an isolated yield ca. 70–90% after 2 h, the reuse of such a complex was compromised due to the partial leaching of osmium.

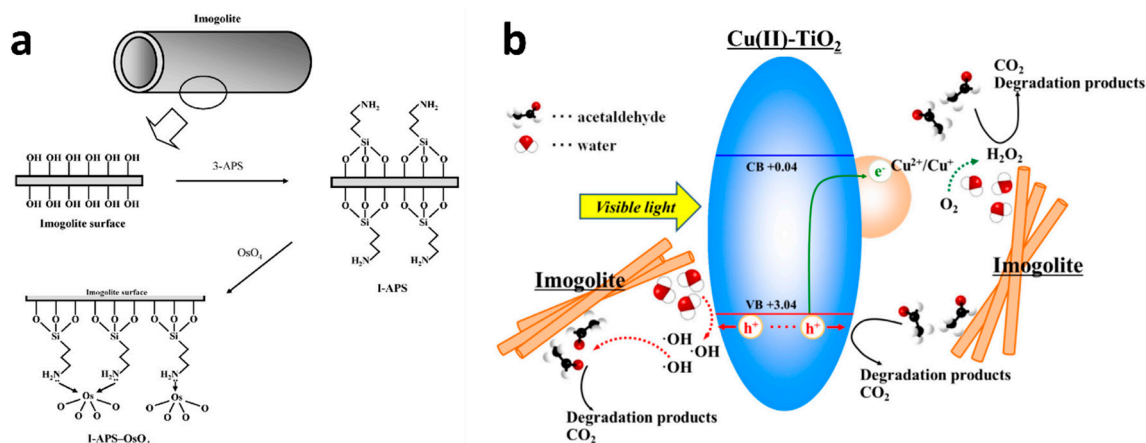


**Figure 14.** (a) Surface-modified imogolite with 3-aminopropyltriethoxysilane (3-APS)–OsO<sub>4</sub> complex for the dihydroxylation of olefins. Adapted with permission from [91]; (b) proposed photodegradation mechanism of acetaldehyde under visible light irradiation by Cu(II)-graftedTiO<sub>2</sub>/INT composite based on (OH)<sub>3</sub>Al<sub>2</sub>O<sub>3</sub>Si(OH). Adapted with permission from [92].

#### 4.2.2. Photocatalysis

The distinctive physico-chemical properties that make INTs (typically with chemical formula SiAl<sub>2</sub>O<sub>4</sub>H<sub>7</sub>) attractive for photocatalytic applications are: tubular structures attributing a bi-functional surface [external octahedron of aluminum (Al) and internal tetrahedron of silicon (Si)], tunable monodisperse diameter, permanent polarization, and real-space separation of the valence band (VB) and the conduction band (CB) edges. One can say that these peculiar nanotubes presenting the mentioned properties may serve as suitable nanoreactors to enhance charge carrier separation and transport path distances across the nanotube walls, which would favor the H<sub>2</sub> production yields. Specifically, one can mention the permanent dipole density at the walls of INTs (either single or double walled) provided by DFT calculations results in an electronegative inner tube, while the outer tube displays an electropositive surface that might promote a permanent polarization that seems to be beneficial for photocatalysis steps. Nevertheless, experimental evidences shall confirm this theoretical prediction. Briefly, for the case of CO<sub>2</sub> reduction, literature points out that one key parameter is the uptake of CO<sub>2</sub> adsorption onto the surface of the catalyst. In this direction, we thus believe that INTs might behave as highly porous structures as analogs to MOF that can benefit the bi-functional surface to enhance CO<sub>2</sub> molecules adsorption, and then the typical photocatalytic steps can take place.

Degradation of organic pollutants is an evolving field within photocatalysis, thermal, and/or chemical activations. With their unique structure, INTs may appeal to address environmental issues. Pristine and Fe-doped INTs with methylated (hydrophobic) inner cavities were tested for the photocatalytic degradation of tartrazine in the presence of H<sub>2</sub>O<sub>2</sub> [93]. Bare methyl-INTs achieved 65% total organic carbon (TOC) removal after 2 h under UV light. However, Fe-doped methyl-INTs (with  $x = 0.025$ ), allowed 90% TOC removal within the same UV irradiation period. Fe-doped INTs saw their band gaps significantly decreased compared to bare INTs, resulting in an improvement of light absorption. A more elaborated approach was reported by Katsumata et al. by grafting Cu(II) onto the TiO<sub>2</sub> surface, which was subsequently coupled with INTs [92]. The successful preparation of this ternary was tested to enhance the removal and the photodegradation of acetaldehyde under visible light irradiation. The authors proposed that imogolite not only adsorbed acetaldehyde but also the intermediate degradation products, which were subsequently degraded by the radical species generated through a photoinduced interfacial charge transfer of electrons from TiO<sub>2</sub> to Cu(II) (Figure 14b). In addition, the decomposition of acetaldehyde into CO<sub>2</sub> seemed to be unaffected by relative humidity, offering a wide range of applications in different environments for this effective visible light-driven photocatalyst composite.

An attractive and promising issue regarding this class of nanotubes is certainly their unique interface polarization. Gustafsson was the first to propose that elongations and shortening of outer Al–O and inner Si–O bonds could be at the origin of a weak positive (negative) charge on the outer (inner) surface of the nanotubes [94]. Teobaldi's group pioneered the DFT calculations applied to INTs on different physico-chemical forms [70]. These simulations confirm that INTs display a permanent dipole surface density  $\mu_\sigma$  (Figure 15a,b). More importantly, INTs present a real-space separation of the valence band and the conduction band edges, which may be beneficial for electron–hole ( $e^-/h^+$ ) separation via optical charge-transfer excitations across the nanotube walls [95]. The forward-looking improvement of  $e^-/h^+$  separation can therefore be effective in sustaining photocatalytic reactivity directly by the nanotube itself [96–98]. Although the computed VB and CB edges and the corresponding energy drive toward photoreduction (or photooxydation) appear to depend weakly on the nanotube diameter and the curvature, the separation of charges in methyl-modified INTs seems to be related to the nature of isomorphous substitution with respect to the inner cavity (Figure 15a,b) [73].

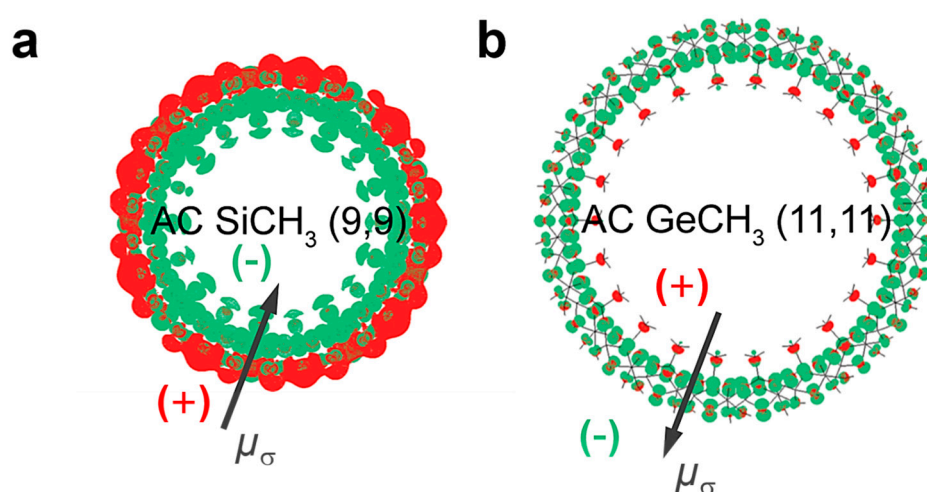


**Figure 15.** Front view of the real-space separation between the valence band (green) and the conduction band (red) edges for armchair methylated INTs  $(\text{OH})_3\text{Al}_2\text{O}_3\text{Y}(\text{CH}_3)$ . (a)  $\text{Y} = \text{Si}$ ; (b)  $\text{Y} = \text{Ge}$ . The black arrow illustrates the direction of the permanent dipole surface density  $\mu_\sigma$  of the nanotube wall. Adapted with permission from [73].

Interestingly, the presence of a second nanotube (double-walled structure) or the role of defects may induce strong changes in the wall polarization [98]. These differences further illustrate the potential of controlling the structure of INTs for finely tuning the electrostatics inside the nanotubes' cavities. This could make imogolite an interesting option for photocatalysis, where the permanent dipole density at the walls of INTs can be exploited for selective reduction/oxidation of different reactants on different sides of the nanotube cavity and to control the overall energy drive and kinetics of the redox event for confined molecules. Hydrogen production and  $\text{CO}_2$  reduction are the leading reactions to evaluate the performance of photocatalytic materials for energy applications [99]. To the best of our knowledge, there is still no report on any of these two reactions by using INTs. Taking advantage of intrinsic polarizability properties and ease of production, the potential of INTs for polarization-enhanced photocatalytic applications will certainly stimulate further experimental investigations in the near future. Therefore, the use of INTs for energy conversion is feasible in the near future, bringing a new type of material into the vast field of photocatalysts.

## 5. Conclusions and Perspectives

Designing efficient photocatalysts with high photo-conversion efficiency is the ultimate goal for photocatalytic  $\text{H}_2$  evolution. This review summarizes some typical routes for the elaboration of high-performance photocatalysts to improve the photo-conversion efficiency. Firstly, the recent

progress in fabricating CuS- and NiS-based heterojunctions for photocatalytic H<sub>2</sub> is summarized. Afterwards, TiO<sub>2</sub> based core-shell structures and periodical structures with excellent adsorption ability are discussed. Lastly, imogolite hollow cylinders are introduced in brief, and their application for photocatalysis is proposed.

Although reasonable research progress was accomplished on the design of photocatalysts with high-conversion efficiency, there are still some issues to be addressed. For example, most metal chalcogenides-based heterojunctions can only split water in the presence of sacrificial agents. Hence, it is very urgent to develop novel metal chalcogenides-based heterojunctions that can split water directly without sacrificial agents. There are two solutions: (1) combining two semiconductors in one heterojunction, which can drive hydrogen and oxygen production; (2) design and preparation of novel metal chalcogenides with more suitable band gap and potential band position. Another issue for metal chalcogenides is that the photocatalytic active sites for H<sub>2</sub> are rarely studied. However, the catalytic sites are very important for us to continue research on catalyst modification and efficiency improvement.

To the best of our knowledge, no studies of photocatalytic H<sub>2</sub> production or CO<sub>2</sub> reduction using INTs have been reported to date. Therefore, the introduction of this emerging material as a suitable nanoreactor due to its semiconductor predicted features should be undertaken. In relation to the challenges of photocatalysis, namely the use of the full spectrum of solar irradiation, two main modification strategies for INTs can be proposed: doping and functionalization. Such issues can be studied by cutting-edge characterization technology along with theoretical calculations, such as in operando X-ray adsorption spectroscopy, Fourier-transform infrared spectroscopy, and transient absorption measurements to provide advanced structure-activity correlations and mechanism explanations.

**Author Contributions:** All authors have contributed equally. All authors have read and agreed to the published version of the manuscript.

**Funding:** Jian Li acknowledges the public grant overseen by the French National Research Agency (ANR) as part of the “Investissements d’Avenir” program (Labex NanoSaclay, reference: ANR-10-LABX-0035) for his post-doc position. Pablo Jimenez-Calvo and Erwan Paineau thank the French ANR agency for financial support (grant number ANR-18-CE09-0001, C3PO).

**Conflicts of Interest:** The authors declare no conflict of interest.

## References

1. Lewis, N.S.; Nocera, D.G. Powering the planet: Chemical challenges in solar energy utilization. *Proc. Natl. Acad. Sci. USA* **2006**, *103*, 15729–15735. [[CrossRef](#)] [[PubMed](#)]
2. Züttel, A.; Remhof, A.; Borgschulte, A.; Friedrichs, O. Hydrogen: The future energy carrier. *Philos. Trans. R. Soc. A Math. Phys. Eng. Sci.* **2010**, *368*, 3329–3342. [[CrossRef](#)] [[PubMed](#)]
3. Lewis, N.S. Toward cost-effective solar energy use. *Science* **2007**, *315*, 798–801. [[CrossRef](#)] [[PubMed](#)]
4. Xu, C.; Anusuyadevi, P.R.; Aymonier, C.; Luque, R.; Marre, S. Nanostructured materials for photocatalysis. *Chem. Soc. Rev.* **2019**, *48*, 3868–3902. [[CrossRef](#)] [[PubMed](#)]
5. Acar, C.; Dincer, I.; Naterer, G.F. Review of photocatalytic water-splitting methods for sustainable hydrogen production. *Int. J. Energy Res.* **2016**, *40*, 1449–1473. [[CrossRef](#)]
6. Zhang, P.; Lou, X.W. Design of Heterostructured Hollow Photocatalysts for Solar-to-Chemical Energy Conversion. *Adv. Mater.* **2019**, *31*. [[CrossRef](#)]
7. Su, T.; Shao, Q.; Qin, Z.; Guo, Z.; Wu, Z. Role of Interfaces in Two-Dimensional Photocatalyst for Water Splitting. *ACS Catal.* **2018**, *8*, 2253–2276. [[CrossRef](#)]
8. Moniz, S.J.A.; Shevlin, S.A.; Martin, D.J.; Guo, Z.-X.; Tang, J. Visible-light driven heterojunction photocatalysts for water splitting—A critical review. *Energy Environ. Sci.* **2015**, *8*, 731–759. [[CrossRef](#)]
9. Selinsky, R.S.; Ding, Q.; Faber, M.S.; Wright, J.C.; Jin, S. Quantum dot nanoscale heterostructures for solar energy conversion. *Chem. Soc. Rev.* **2013**, *42*, 2963–2985. [[CrossRef](#)]
10. Gao, X.; Li, J.; Du, R.; Zhou, J.; Huang, M.-Y.; Liu, R.; Li, J.; Xie, Z.; Wu, L.-Z.; Liu, Z.; et al. Direct Synthesis of Graphdiyne Nanowalls on Arbitrary Substrates and Its Application for Photoelectrochemical Water Splitting Cell. *Adv. Mater.* **2017**, *29*. [[CrossRef](#)]

11. Li, J.; Gao, X.; Liu, B.; Feng, Q.; Li, X.-B.; Huang, M.-Y.; Liu, Z.; Zhang, J.; Tung, C.-H.; Wu, L.-Z. Graphdiyne: A Metal-Free Material as Hole Transfer Layer to Fabricate Quantum Dot-Sensitized Photocathodes for Hydrogen Production. *J. Am. Chem. Soc.* **2016**, *138*, 3954–3957. [[CrossRef](#)] [[PubMed](#)]
12. Marschall, R. Semiconductor Composites: Strategies for Enhancing Charge Carrier Separation to Improve Photocatalytic Activity. *Adv. Funct. Mater.* **2014**, *24*, 2421–2440. [[CrossRef](#)]
13. Yuan, Y.-P.; Ruan, L.-W.; Barber, J.; Loo, S.C.J.; Xue, C. Hetero-nanostructured suspended photocatalysts for solar-to-fuel conversion. *Energy Environ. Sci.* **2014**, *7*, 3934–3951. [[CrossRef](#)]
14. Li, J.-X.; Li, Z.-J.; Ye, C.; Li, X.-B.; Zhan, F.; Fan, X.-B.; Li, J.; Chen, B.; Tao, Y.; Tung, C.-H.; et al. Visible light-induced photochemical oxygen evolution from water by 3,4,9,10-perylenetetracarboxylic dianhydride nanorods as an n-type organic semiconductor. *Catal. Sci. Technol.* **2016**, *6*, 672–676. [[CrossRef](#)]
15. Zhong, M.; Hisatomi, T.; Kuang, Y.; Zhao, J.; Liu, M.; Iwase, A.; Jia, Q.; Nishiyama, H.; Minegishi, T.; Nakabayashi, M.; et al. Surface Modification of CoO<sub>x</sub> Loaded BiVO<sub>4</sub> Photoanodes with Ultrathin p-Type NiO Layers for Improved Solar Water Oxidation. *J. Am. Chem. Soc.* **2015**, *137*, 5053–5060. [[CrossRef](#)]
16. Zhang, K.; Guo, L. Metal sulphide semiconductors for photocatalytic hydrogen production. *Catal. Sci. Technol.* **2013**, *3*, 1672–1690. [[CrossRef](#)]
17. Nie, L.; Zhang, Q. Recent progress in crystalline metal chalcogenides as efficient photocatalysts for organic pollutant degradation. *Inorg. Chem. Front.* **2017**, *4*, 1953–1962. [[CrossRef](#)]
18. Borgarello, E.; Kalyanasundaram, K.; Grätzel, M.; Pelizzetti, E. Visible Light-Induced Generation of Hydrogen from H<sub>2</sub>S in CdS Dispersions; Hole Transfer Catalysis by RuO<sub>2</sub>. *Helv. Chim. Acta* **1982**, *65*, 243–248. [[CrossRef](#)]
19. Gesesse, G.D.; Li, C.; Paineau, E.; Habibi, Y.; Remita, H.; Colbeau-Justin, C.; Ghazzal, M.N. Enhanced Photogenerated Charge Carriers and Photocatalytic Activity of Biotemplated Mesoporous TiO<sub>2</sub> Films with a Chiral Nematic Structure. *Chem. Mater.* **2019**, *31*, 4851–4863. [[CrossRef](#)]
20. Gesesse, G.D.; le Neel, T.; Cui, Z.; Bachelier, G.; Remita, H.; Colbeau-Justin, C.; Ghazzal, M.N. Plasmonic core-shell nanostructure as an optical photoactive nanolens for enhanced light harvesting and hydrogen production. *Nanoscale* **2018**, *10*, 20140–20146. [[CrossRef](#)]
21. Li, J.; Gao, X.; Li, Z.; Wang, J.-H.; Zhu, L.; Yin, C.; Wang, Y.; Li, X.-B.; Liu, Z.; Zhang, J.; et al. Superhydrophilic Graphdiyne Accelerates Interfacial Mass/Electron Transportation to Boost Electrochemical and Photoelectrocatalytic Water Oxidation Activity. *Adv. Funct. Mater.* **2019**, *29*. [[CrossRef](#)]
22. Li, X.; Yu, J.; Low, J.; Fang, Y.; Xiao, J.; Chen, X. Engineering heterogeneous semiconductors for solar water splitting. *J. Mater. Chem. A* **2015**, *3*, 2485–2534. [[CrossRef](#)]
23. Wang, H.; Zhang, L.; Chen, Z.; Hu, J.; Li, S.; Wang, Z.; Liu, J.; Wang, X. Semiconductor heterojunction photocatalysts: Design, construction, and photocatalytic performances. *Chem. Soc. Rev.* **2014**, *43*, 5234–5244. [[CrossRef](#)] [[PubMed](#)]
24. Li, J.; Gao, X.; Jiang, X.; Li, X.-B.; Liu, Z.; Zhang, J.; Tung, C.-H.; Wu, L.-Z. Graphdiyne: A Promising Catalyst-Support to Stabilize Cobalt Nanoparticles for Oxygen Evolution. *ACS Catal.* **2017**, *7*, 5209–5213. [[CrossRef](#)]
25. Prakash, A.; Dan, M.; Yu, S.; Wei, S.; Li, Y.; Wang, F.; Zhou, Y. In<sub>2</sub>S<sub>3</sub>/CuS nanosheet composite: An excellent visible light photocatalyst for H<sub>2</sub> production from H<sub>2</sub>S. *Sol. Energy Mater. Sol. Cells* **2018**, *180*, 205–212. [[CrossRef](#)]
26. Li, N.; Fu, W.; Chen, C.; Liu, M.; Xue, F.; Shen, Q.; Zhou, J. Controlling the Core-Shell Structure of CuS@CdS Heterojunction via Seeded Growth with Tunable Photocatalytic Activity. *ACS Sustain. Chem. Eng.* **2018**, *6*, 15867–15875. [[CrossRef](#)]
27. Zhang, J.; Yu, J.; Zhang, Y.; Li, Q.; Gong, J.R. Visible Light Photocatalytic H<sub>2</sub>-Production Activity of CuS/ZnS Porous Nanosheets Based on Photoinduced Interfacial Charge Transfer. *Nano Lett.* **2011**, *11*, 4774–4779. [[CrossRef](#)]
28. Huang, J.; Shi, Z.; Dong, X. Nickel sulfide modified TiO<sub>2</sub> nanotubes with highly efficient photocatalytic H<sub>2</sub> evolution activity. *J. Energy Chem.* **2016**, *25*, 136–140. [[CrossRef](#)]
29. Qiao, P.; Wu, J.; Li, H.; Xu, Y.; Sun, B.; Ren, L.; Pan, K.; Wang, L.; Zhou, W. Improved charge separation of NiS nanoparticles modified defect-engineered black TiO<sub>2</sub> hollow nanotubes for boosting solar-driven photocatalytic H<sub>2</sub> evolution. *Nanotechnology* **2019**, *30*, 125703. [[CrossRef](#)]
30. Li, C.; Wang, H.; Naghadeh, S.B.; Zhang, J.Z.; Fang, P. Visible light driven hydrogen evolution by photocatalytic reforming of lignin and lactic acid using one-dimensional NiS/CdS nanostructures. *Appl. Catal. B* **2018**, *227*, 229–239. [[CrossRef](#)]

31. Wei, L.; Chen, Y.; Zhao, J.; Li, Z. Preparation of NiS/ZnIn<sub>2</sub>S<sub>4</sub> as a superior photocatalyst for hydrogen evolution under visible light irradiation. *Beilstein J. Nanotechnol.* **2013**, *4*, 949–955. [[CrossRef](#)] [[PubMed](#)]
32. Xia, Y.; Liang, S.; Wu, L.; Wang, X. Ultrasmall NiS decorated HNb<sub>3</sub>O<sub>8</sub> nanosheets as highly efficient photocatalyst for H<sub>2</sub> evolution reaction. *Catal. Today* **2019**, *330*, 195–202. [[CrossRef](#)]
33. Zhao, X.; Feng, J.; Liu, J.; Shi, W.; Yang, G.; Wang, G.C.; Cheng, P. An Efficient, Visible-Light-Driven, Hydrogen Evolution Catalyst NiS/Zn<sub>x</sub>Cd<sub>1-x</sub>S Nanocrystal Derived from a Metal-Organic Framework. *Angew. Chem. Int. Ed. Engl.* **2018**, *57*, 9790–9794. [[CrossRef](#)] [[PubMed](#)]
34. Hong, J.; Wang, Y.; Wang, Y.; Zhang, W.; Xu, R. Noble-metal-free NiS/C<sub>3</sub>N<sub>4</sub> for efficient photocatalytic hydrogen evolution from water. *ChemSusChem* **2013**, *6*, 2263–2268. [[CrossRef](#)] [[PubMed](#)]
35. Lim, W.Y.; Wu, H.; Lim, Y.-F.; Ho, G.W. Facilitating the charge transfer of ZnMoS<sub>4</sub>/CuS p–n heterojunctions through ZnO intercalation for efficient photocatalytic hydrogen generation. *J. Mater. Chem. A* **2018**, *6*, 11416–11423. [[CrossRef](#)]
36. Chen, X.; Li, L.; Zhang, W.; Li, Y.; Song, Q.; Dong, L. Fabricate Globular Flower-like CuS/CdIn<sub>2</sub>S<sub>4</sub>/ZnIn<sub>2</sub>S<sub>4</sub> with High Visible Light Response via Microwave-assisted One-step Method and Its Multipathway Photoelectron Migration Properties for Hydrogen Evolution and Pollutant Degradation. *ACS Sustain. Chem. Eng.* **2016**, *4*, 6680–6688. [[CrossRef](#)]
37. Li, N.; Huang, H.; Bibi, R.; Shen, Q.; Ngulube, R.; Zhou, J.; Liu, M. Noble-metal-free MOF derived hollow CdS/TiO<sub>2</sub> decorated with NiS cocatalyst for efficient photocatalytic hydrogen evolution. *Appl. Surf. Sci.* **2019**, *476*, 378–386. [[CrossRef](#)]
38. Wang, B.; Ding, Y.; Deng, Z.; Li, Z. Rational design of ternary NiS/CQDs/ZnIn<sub>2</sub>S<sub>4</sub> nanocomposites as efficient noble-metal-free photocatalyst for hydrogen evolution under visible light. *Chin. J. Catal.* **2019**, *40*, 335–342. [[CrossRef](#)]
39. Wei, R.-B.; Huang, Z.-L.; Gu, G.-H.; Wang, Z.; Zeng, L.; Chen, Y.; Liu, Z.-Q. Dual-cocatalysts decorated rimous CdS spheres advancing highly-efficient visible-light photocatalytic hydrogen production. *Appl. Catal. B* **2018**, *231*, 101–107. [[CrossRef](#)]
40. Yang, X.; Cao, C.; Erickson, L.; Hohn, K.; Maghirang, R.; Klabunde, K. Photo-catalytic degradation of Rhodamine B on C-, S-, N-, and Fe-doped TiO<sub>2</sub> under visible-light irradiation. *Appl. Catal. B* **2009**, *91*, 657–662. [[CrossRef](#)]
41. Asahi, R.; Morikawa, T.; Ohwaki, T.; Aoki, K.; Taga, Y. Visible-Light Photocatalysis in Nitrogen-Doped Titanium Oxides. *Science* **2001**, *293*, 269–271. [[CrossRef](#)] [[PubMed](#)]
42. In, S.; Orlov, A.; Berg, R.; García, F.; Pedrosa-Jimenez, S.; Tikhov, M.S.; Wright, D.S.; Lambert, R.M. Effective Visible Light-Activated B-Doped and B,N-Codoped TiO<sub>2</sub> Photocatalysts. *J. Am. Chem. Soc.* **2007**, *129*, 13790–13791. [[CrossRef](#)] [[PubMed](#)]
43. Umebayashi, T.; Yamaki, T.; Itoh, H.; Asai, K. Band gap narrowing of titanium dioxide by sulfur doping. *Appl. Phys. Lett.* **2002**, *81*, 454–456. [[CrossRef](#)]
44. Chatterjee, D.; Mahata, A. Visible light induced photodegradation of organic pollutants on dye adsorbed TiO<sub>2</sub> surface. *J. Photochem. Photobiol. A* **2002**, *153*, 199–204. [[CrossRef](#)]
45. Abe, R.; Hara, K.; Sayama, K.; Domen, K.; Arakawa, H. Steady hydrogen evolution from water on Eosin Y-fixed TiO<sub>2</sub> photocatalyst using a silane-coupling reagent under visible light irradiation. *J. Photochem. Photobiol. A* **2000**, *137*, 63–69. [[CrossRef](#)]
46. Nehme, A.S.; Haydous, F.; Halaoui, L. Amplification in Light Energy Conversion at Q-CdTe Sensitized TiO<sub>2</sub> Photonic Crystal, Photoelectrochemical Stability in Se<sup>2-</sup> Electrolyte, and Size-Dependent Type II Q-CdTe/CdSe Formation. *J. Phys. Chem. C* **2016**, *120*, 4766–4778. [[CrossRef](#)]
47. Bessekhoad, Y.; Chaoui, N.; Trzpit, M.; Ghazzal, N.; Robert, D.; Weber, J.V. UV-vis versus visible degradation of Acid Orange II in a coupled CdS/TiO<sub>2</sub> semiconductors suspension. *J. Photochem. Photobiol. A* **2006**, *183*, 218–224. [[CrossRef](#)]
48. Park, H.; Choi, W.; Hoffmann, M.R. Effects of the preparation method of the ternary CdS/TiO<sub>2</sub>/Pt hybrid photocatalysts on visible light-induced hydrogen production. *J. Mater. Chem.* **2008**, *18*, 2379–2385. [[CrossRef](#)]
49. Chen, J.I.L.; von Freymann, G.; Choi, S.Y.; Kitaev, V.; Ozin, G.A. Slow photons in the fast lane in chemistry. *J. Mater. Chem.* **2008**, *18*, 369–373. [[CrossRef](#)]
50. Yablonoitch, E. Inhibited Spontaneous Emission in Solid-State Physics and Electronics. *Phys. Rev. Lett.* **1987**, *58*, 2059–2062. [[CrossRef](#)]

51. Deparis, O.; Vigneron, J.P. Modeling the photonic response of biological nanostructures using the concept of stratified medium: The case of a natural three-dimensional photonic crystal. *Mater. Sci. Eng. B* **2010**, *169*, 12–15. [[CrossRef](#)]
52. Vukusic, P.; Sambles, J.R. Photonic structures in biology. *Nature* **2003**, *424*, 852–855. [[CrossRef](#)] [[PubMed](#)]
53. Ghazzal, M.N.; Deparis, O.; Errachid, A.; Kebaili, H.; Simonis, P.; Eloy, P.; Vigneron, J.P.; de Coninck, J.; Gaigneaux, E.M. Porosity control and surface sensitivity of titania/silica mesoporous multilayer coatings: Applications to optical Bragg resonance tuning and molecular sensing. *J. Mater. Chem.* **2012**, *22*, 25302–25310. [[CrossRef](#)]
54. Ghazzal, M.N.; Deparis, O.; de Coninck, J.; Gaigneaux, E.M. Tailored refractive index of inorganic mesoporous mixed-oxide Bragg stacks with bio-inspired hygrochromic optical properties. *J. Mater. Chem. C* **2013**, *1*, 6202–6209. [[CrossRef](#)]
55. Aguirre, C.I.; Reguera, E.; Stein, A. Tunable Colors in Opals and Inverse Opal Photonic Crystals. *Adv. Funct. Mater.* **2010**, *20*, 2565–2578. [[CrossRef](#)]
56. Mekis, A.; Chen, J.C.; Kurland, I.; Fan, S.; Villeneuve, P.R.; Joannopoulos, J.D. High Transmission through Sharp Bends in Photonic Crystal Waveguides. *Phys. Rev. Lett.* **1996**, *77*, 3787–3790. [[CrossRef](#)]
57. Ghazzal, M.N.; Joseph, M.; Kebaili, H.; de Coninck, J.; Gaigneaux, E.M. Tuning the selectivity and sensitivity of mesoporous dielectric multilayers by modifying the hydrophobic–hydrophilic balance of the silica layer. *J. Mater. Chem.* **2012**, *22*, 22526–22532. [[CrossRef](#)]
58. Puzzo, D.P.; Scotognella, F.; Zavelani-Rossi, M.; Sebastian, M.; Lough, A.J.; Manners, I.; Lanzani, G.; Tubino, R.; Ozin, G.A. Distributed Feedback Lasing from a Composite Poly(phenylene vinylene)–Nanoparticle One-Dimensional Photonic Crystal. *Nano Lett.* **2009**, *9*, 4273–4278. [[CrossRef](#)]
59. Zhang, X.; Liu, Y.; Lee, S.-T.; Yang, S.; Kang, Z. Coupling surface plasmon resonance of gold nanoparticles with slow-photon-effect of TiO<sub>2</sub> photonic crystals for synergistically enhanced photoelectrochemical water splitting. *Energy Environ. Sci.* **2014**, *7*, 1409–1419. [[CrossRef](#)]
60. Park, H.G.; Jung, Y. Carbon nanofluidics of rapid water transport for energy applications. *Chem. Soc. Rev.* **2014**, *43*, 565–576. [[CrossRef](#)]
61. Miners, S.A.; Rance, G.A.; Khlobystov, A.N. Chemical reactions confined within carbon nanotubes. *Chem. Soc. Rev.* **2016**, *45*, 4727–4746. [[CrossRef](#)] [[PubMed](#)]
62. Iglesias, D.; Melchionna, M. Enter the Tubes: Carbon Nanotube Endohedral Catalysis. *Catalysts* **2019**, *9*, 128. [[CrossRef](#)]
63. Huang, H.; Tu, S.; Zeng, C.; Zhang, T.; Reshak, A.H.; Zhang, Y. Macroscopic Polarization Enhancement Promoting Photo- and Piezoelectric-Induced Charge Separation and Molecular Oxygen Activation. *Angew. Chem. Int. Ed.* **2017**, *56*, 11860–11864. [[CrossRef](#)] [[PubMed](#)]
64. Chen, F.; Huang, H.; Guo, L.; Zhang, Y.; Ma, T. The Role of Polarization in Photocatalysis. *Angew. Chem. Int. Ed.* **2019**, *58*, 10061–10073. [[CrossRef](#)] [[PubMed](#)]
65. Paineau, E. Imogolite Nanotubes: A Flexible Nanoplatfrom with Multipurpose Applications. *Appl. Sci.* **2018**, *8*, 1921. [[CrossRef](#)]
66. Paineau, E.; Launois, P. Nanomaterials from Imogolite: Structure, Properties, and Functional Materials. In *Nanomaterials from Clay Minerals*; Elsevier: Amsterdam, The Netherlands, 2019; pp. 257–284.
67. Yoshinaga, N.; Aomine, S. Imogolite in some ando soils. *Soil Sci. Plant Nutr.* **1962**, *8*, 22–29. [[CrossRef](#)]
68. Farmer, V.; Fraser, A.; Tait, J.M. Synthesis of Imogolite: A Tubular Aluminium Silicate Polymer. *J. Chem. Soc. Chem. Commun.* **1977**, *12*, 462–463. [[CrossRef](#)]
69. Guimaraes, L.; Enyashin, A.N.; Frenzel, J.; Heine, T.; Duarte, H.A.; Seifert, G. Imogolite Nanotubes: Stability, Electronic, and Mechanical Properties. *ACS Nano* **2007**, *1*, 362–368. [[CrossRef](#)]
70. Teobaldi, G.; Beglitis, N.S.; Fisher, A.J.; Zerbetto, F.; Hofer, A.A. Hydroxyl vacancies in single-walled aluminosilicate and aluminogermanate nanotubes. *J. Phys. Condens. Matter* **2009**, *21*. [[CrossRef](#)]
71. Maillet, P.; Levard, C.; Spalla, O.; Masion, A.; Rose, J.; Thill, A. Growth kinetic of single and double-walled aluminogermanate imogolite-like nanotubes: An experimental and modeling approach. *Phys. Chem. Chem. Phys.* **2011**, *13*, 2682–2689. [[CrossRef](#)]
72. Yucelen, G.I.; Kang, D.-Y.; Schmidt-Krey, I.; Beckham, H.W.; Nair, S. A generalized kinetic model for the formation and growth of single-walled metal oxide nanotubes. *Chem. Eng. Sci.* **2013**, *90*, 200–212. [[CrossRef](#)]

73. Monet, G.; Amara, M.S.; Rouzière, S.; Paineau, E.; Chai, Z.; Elliott, J.D.; Poli, E.; Liu, L.-M.; Teobaldi, G.; Launois, P. Structural resolution of inorganic nanotubes with complex stoichiometry. *Nat. Commun.* **2018**, *9*, 2033. [[CrossRef](#)] [[PubMed](#)]
74. Yucelen, G.I.; Kang, D.-Y.; Guerrero-Ferreira, R.C.; Wright, E.R.; Beckham, H.W.; Nair, S. Shaping Single-Walled Metal Oxide Nanotubes from Precursors of Controlled Curvature. *Nano Lett.* **2012**, *12*, 827–832. [[CrossRef](#)] [[PubMed](#)]
75. Thill, A.; Guiose, B.; Bacia-Verloop, M.; Geertsen, V.; Belloni, L. How the Diameter and Structure of  $(\text{OH})_3\text{Al}_2\text{O}_3\text{Si}_x\text{Ge}_{1-x}\text{OH}$  Imogolite Nanotubes Are Controlled by an Adhesion versus Curvature Competition. *J. Phys. Chem. C* **2012**, *116*, 26841–26849. [[CrossRef](#)]
76. Amara, M.-S.; Paineau, E.; Bacia-Verloop, M.; Krapf, M.-E.M.; Davidson, P.; Belloni, L.; Levard, C.; Rose, J.; Launois, P.; Thill, A. Single-step formation of micron long  $(\text{OH})_3\text{Al}_2\text{O}_3\text{Ge}(\text{OH})$  imogolite-like nanotubes. *Chem. Commun.* **2013**, *49*, 11284–11286. [[CrossRef](#)]
77. Amara, M.S.; Paineau, E.; Rouzière, S.; Guiose, B.; Krapf, M.-E.M.; Taché, O.; Launois, P.; Thill, A. Hybrid, Tunable-Diameter, Metal Oxide Nanotubes for Trapping of Organic Molecules. *Chem. Mater.* **2015**, *27*, 1488–1494. [[CrossRef](#)]
78. Chemmi, A.; Brendle, J.; Marichal, C.; Lebeau, B. Key Steps Influencing the Formation of Aluminosilicate Nanotubes by the Fluoride Route. *Clays Clay Miner.* **2015**, *63*, 132–143. [[CrossRef](#)]
79. Picot, P.; Gobeaux, F.; Coradin, T.; Thill, A. Dual internal functionalization of imogolite nanotubes as evidenced by optical properties of Nile red. *Appl. Clay Sci.* **2019**, *178*, 105133. [[CrossRef](#)]
80. Arancibia-Miranda, N.; Escudey, M. Imogolite-Like Family. In *Developments in Clay Science*; Elsevier: Amsterdam, The Netherlands, 2016; Volume 7, pp. 458–483.
81. Farmer, V.; Adams, M.; Fraser, A.; Palmieri, F. Synthetic imogolite: Properties synthesis and possible applications. *Clay Miner.* **1983**, *18*, 459–472. [[CrossRef](#)]
82. Van Nordstrand, R.A. Hydrocarbons Hydroprocessing with Imogolite Catalyst. U.S. Patent 4394253, 19 July 1983.
83. Imamura, S.; Hayashi, Y.; Kajiwara, K.; Hoshino, H.; Kaito, C. Imogolite: A possible new type of shape-selective catalyst. *Ind. Eng. Chem. Res.* **1993**, *32*, 600–603. [[CrossRef](#)]
84. Ookawa, M.; Onishi, Y.; Fukukawa, S.-I.; Matsumoto, K.-I.; Watanabe, M.; Yamaguchi, T.; Suzuki, M.J. Catalytic Property of Synthetic Imogolite. *Clay Sci. Soc. Jpn.* **2006**, *45*, 184–187. (In Japanese)
85. Olson, N.; Deshpande, N.; Gunduz, S.; Ozkan, U.S.; Brunelli, N.A. Utilizing imogolite nanotubes as a tunable catalytic material for the selective isomerization of glucose to fructose. *Catal. Today* **2019**, *323*, 69–75. [[CrossRef](#)]
86. Shafia, E.; Esposito, S.; Manzoli, M.; Chiesa, M.; Tiberto, P.; Barrera, G.; Menard, G.; Allia, P.; Freyria, F.S.; Garrone, E.; et al. Al/Fe isomorphic substitution versus  $\text{Fe}_2\text{O}_3$  clusters formation in Fe-doped aluminosilicate nanotubes (imogolite). *J. Nanopart. Res.* **2015**, *17*, 336. [[CrossRef](#)]
87. Ookawa, M.; Inoue, Y.; Watanabe, M.; Suzuki, M.; Yamaguchi, T. Synthesis and Characterization of Fe Containing Imogolite. *Clay Sci.* **2006**, *12*, 280–284.
88. Ookawa, M.; Takata, Y.; Suzuki, M.; Inukai, K.; Maekawa, T.; Yamaguchi, T. Oxidation of aromatic hydrocarbons with  $\text{H}_2\text{O}_2$  catalyzed by a nano-scale tubular aluminosilicate, Fe-containing imogolite. *Res. Chem. Intermed.* **2008**, *34*, 679–685. [[CrossRef](#)]
89. Shafia, E.; Esposito, S.; Armandi, M.; Bahadori, E.; Garrone, E.; Bonelli, B. Reactivity of bare and Fe-doped alumino-silicate nanotubes (imogolite) with  $\text{H}_2\text{O}_2$  and the azo-dye Acid Orange 7. *Catal. Today* **2016**, *277*, 89–96. [[CrossRef](#)]
90. Imamura, S.; Kokubu, T.; Yamashita, T.; Okamoto, Y.; Kajiwara, K.; Kanai, H. Shape-selective copper-loaded Imogolite catalyst. *J. Catal.* **1996**, *160*, 137–139. [[CrossRef](#)]
91. Qi, X.; Yoon, H.; Lee, S.-H.; Yoon, J.; Kim, S.-J. Surface-modified imogolite by 3-APS- $\text{OsO}_4$  complex: Synthesis, characterization and its application in the dihydroxylation of olefins. *J. Ind. Eng. Chem.* **2008**, *14*, 136–141. [[CrossRef](#)]
92. Katsumata, K.-I.; Hou, X.; Sakai, M.; Nakajima, A.; Fujishima, A.; Matsushita, N.; MacKenzie, K.J.D.; Okada, K. Visible-light-driven photodegradation of acetaldehyde gas catalyzed by aluminosilicate nanotubes and Cu(II)-grafted  $\text{TiO}_2$  composites. *Appl. Catal. B Environ.* **2013**, *138*, 243–252. [[CrossRef](#)]

93. Bahadori, E.; Vaiano, V.; Esposito, S.; Armandi, M.; Sannino, D.; Bonelli, B. Photo-activated degradation of tartrazine by H<sub>2</sub>O<sub>2</sub> as catalyzed by both bare and Fe-doped methyl-imogolite nanotubes. *Catal. Today* **2018**, *304*, 199–207. [[CrossRef](#)]
94. Gustafsson, J.P. The surface chemistry of imogolite. *Clays Clay Miner.* **2001**, *49*, 73–80. [[CrossRef](#)]
95. Poli, E.; Elliott, J.D.; Hine, N.D.M.; Mostofi, A.A.; Teobaldi, G. Large-scale density functional theory simulation of inorganic nanotubes: A case study on Imogolite nanotubes. *Mater. Res. Innov.* **2015**, *19*, S272–S282. [[CrossRef](#)]
96. Poli, E.; Elliott, J.D.; Ratcliff, L.E.; Andrinopoulos, L.; Dziedzic, J.; Hine, N.D.M.; Mostofi, A.A.; Skylaris, C.-K.; Haynes, P.D.; Teobaldi, G. The potential of imogolite nanotubes as (co-)photocatalysts: A linear-scaling density functional theory study. *J. Phys. Condens. Matter* **2016**, *28*, 074003. [[CrossRef](#)]
97. Elliott, J.D.; Poli, E.; Scivetti, I.; Ratcliff, L.E.; Andrinopoulos, L.; Dziedzic, J.; Hine, N.D.M.; Mostofi, A.A.; Skylaris, C.-K.; Haynes, P.D.; et al. Chemically Selective Alternatives to Photoferroelectrics for Polarization-Enhanced Photocatalysis: The Untapped Potential of Hybrid Inorganic Nanotubes. *Adv. Sci.* **2017**, *4*, 1600153. [[CrossRef](#)]
98. Poli, E.; Elliott, J.D.; Chulkov, S.K.; Watkins, M.B.; Teobaldi, G. The role of cation-vacancies for the electronic and optical properties of aluminosilicate imogolite nanotubes: A non-local, linear-response TDDFT study. *Front. Chem.* **2019**, *7*, 210. [[CrossRef](#)]
99. Christoforidis, K.C.; Fornasiero, P. Photocatalysis for Hydrogen Production and CO<sub>2</sub> Reduction: The Case of Copper-Catalysts. *ChemCatChem* **2019**, *11*, 368–382. [[CrossRef](#)]



© 2020 by the authors. Licensee MDPI, Basel, Switzerland. This article is an open access article distributed under the terms and conditions of the Creative Commons Attribution (CC BY) license (<http://creativecommons.org/licenses/by/4.0/>).